Investigating the Near-Surface Wind Fields of Downbursts Using a Series of High-Resolution Idealized Simulations

ANDREW MOORE[a]

[a] *NOAA/NCEP/Storm Prediction Center, Norman, Oklahoma*

(Manuscript received 27 September 2023, in final form 13 April 2024, accepted 1 May 2024)

ABSTRACT: Short-lived and poorly organized convective cells, often called weakly forced thunderstorms (WFTs), are a common phenomenon during the warm season across the eastern and southeastern United States. While typically benign, wet downbursts emanating from such convection can have substantial societal impacts, including tree, power line, and property damage from strong outflow winds. Observational studies have documented the occurrence of severe (25.7 m s^{-1} or higher) wind speeds from wet downbursts, but the frequency of severe downbursts, including the spatial extent and temporal duration of severe winds, remains unclear. The ability for modern observing networks to reliably observe such events is also unknown; however, answering these questions is important for improving forecast skill and verifying convective warnings accurately. This study attempts to answer these questions by drawing statistical inferences from 97 high-resolution idealized simulations of single-cell downburst events. It was found that while 35% of the simulations featured severe winds, the spatial and temporal extent of such winds is limited—$O(10)$ km^2 or less and persisting for around 5 min on average. Furthermore, through a series of simulated network experiments, it is postulated that the probability that a modern mesonet observes a severe wind gust given a severe downburst is around 1%. From these results, a statistical argument is made that most tree impacts associated with pulse convection are likely caused by subsevere winds. Several implications for forecasting, warning, and verifying WFT events fall out from these discussions.

KEYWORDS: Convective storms; Forecasting; Operational forecasting; Probability forecasts/models/distribution; Cloud-resolving models; Idealized models

1. Introduction

Microbursts and macrobursts (hereafter collectively referred to as downbursts) emanating from weakly forced thunderstorms (WFTs; Miller and Mote 2017a) are a well-documented hazard to the aviation and wind engineering communities as well as society at large due to the erratic low-level wind shear and strong winds capable of tree and structural damage associated with the thunderstorm outflow (Fujita 1981a; NTSB 1986; Fujita 1990; Schoen and Ashley 2011). Downbursts are formally described as an intense downdraft emanating from convection that rapidly spreads out radially upon reaching the surface (Fujita 1990). The starburst outflow pattern typically observed with downbursts can pose wind risks away from the primary downdraft, including areas displaced well outside of the parent storm's path. Downbursts can occur in clusters or in isolation and are often categorized based on the diameter of their outflow: 4 km or less is deemed a microburst, while >4 km is considered a macroburst (Fujita 1981b). More concentrated "burst swaths" may occur within a downburst and are typically on the order of around 100 m (Fujita 1981b). These swaths often feature the most intense horizontal winds, which have been documented exceeding the National Weather Service (NWS) severe (SVR) thunderstorm warning criteria [25.7 m s^{-1} or 50 kt (1 kt ≈ 0.51 m s^{-1}), hereafter rounded to 26 m s^{-1} for simplicity] [Fujita and Wakimoto 1981; Wakimoto 1985; Caracena and Maier 1987; Atkins and Wakimoto 1991 (hereafter AW91); Wheeler and Spratt 1995]. In rare cases, downburst winds have been observed up to 67 m s^{-1} (Fujita 1985).

Romanic et al. (2022) found that downburst environments were most common during the summer months across the southwest and southeastern United States when conditioned on lightning occurrence, though the thermodynamic environments and storm morphologies of these two regions can differ considerably. Dry downbursts [downbursts in which precipitation does not reach the surface (Wakimoto 1985)] are more common across the High Plains and southwest due to the propensity for warmer, drier surface conditions and steeper midlevel lapse rates emanating off the nearby terrain. These thermodynamic conditions promote deep, well-mixed boundary layers favorable for evaporating falling precipitation (McCarthy et al. 1982; Wakimoto 1985). Southeast downburst environments are typically characterized by higher moisture content (i.e., greater surface dewpoints and precipitable water values) due to closer proximity to the Gulf of Mexico, resulting in lower cloud bases and shallower subcloud layers compared to dry downburst environments (AW91). As a result, most downbursts across the southeast feature precipitation reaching the surface and are considered "wet" downbursts.

Motivated by a series of fatal airliner accidents due to downburst events, multiple field campaigns during the late 1970s and 1980s documented the low-level flow patterns associated with both wet and dry downbursts as well as the morphology of the parent thunderstorm and the convective environment (Fujita 1978; McCarthy et al. 1982; Dodge et al. 1986; Rinehart and Isaminger 1986; Caracena and Maier 1987). The results from these field studies were expanded upon by subsequent data analyses (Hjelmfelt 1988; Wakimoto

Corresponding author: Andrew Moore, andrew.moore@noaa.gov

DOI: 10.1175/WAF-D-23-0164.1

TABLE 1. Average station spacing of various U.S. surface observing networks.

Network	Average station spacing	Reference
ASOS/AWOS network	44 km	Horel et al. (2002)
West Texas Mesonet	35 km	Schroeder et al. (2005)
Oklahoma Mesonet	30 km	Brock et al. (1995), McPherson et al. (2007)
New York State Mesonet	27 km	Brotzge et al. (2020)
MesoWest	15 km	Horel et al. (2002)
ARS Micronet	5 km	Fiebrich and Crawford (2001)
Oklahoma City Micronet	3 km	Basara et al. (2011)
CINDE Micronet	2–10 km	Wilson et al. (1988)
Recommended	10–25 km	Dabberdt et al. (2005)

and Bringi 1988; Kingsmill and Wakimoto 1991; Lee et al. 1992; Wakimoto et al. 1994) and numerical simulations (Proctor 1988, 1989, 1994; Orf and Anderson 1999; Chay et al. 2006; Kim and Hangan 2007; Mason et al. 2009; Anabor et al. 2011; Orf et al. 2012; Oreskovic et al. 2018), which provided further insight into the near-surface flow patterns of downbursts and the mechanisms by which they occurred.

This early work laid the foundation for a number of convective parameters and indices that attempt to forecast the occurrence of downbursts to alert aircraft of low-level shear and aid in severe wind forecasting (Wakimoto 1985; AW91; McCann 1994; Pryor and Ellrod 2005; Pryor 2015; Romanic et al. 2022). While some work has been done to explicitly forecast maximum wind speeds from downbursts (Foster 1958), many of these parameters were designed with a focus on the aviation community given the history of downburst-related air disasters rather than aiding in severe wind forecasting. Consequently, forecasting the occurrence of severe downbursts from WFTs remains a challenge for both operational severe weather forecasts (Guillot et al. 2008; Herman et al. 2018) and numerical weather prediction (Jirak et al. 2014; Lagerquist et al. 2017; Bolgiani et al. 2020).

One possible reason for this operational challenge is the potential for mischaracterization of downburst events and their respective environments. Many of the surface observing networks employed by these early field campaigns were on the mesogamma scale (2–200 km) with an average station separation of 2–4 km. While this spatial scale is adequate to capture the broad nature of downburst outflows, it may be too coarse to capture the burst swaths that have been documented on the misoscale (10^{-1}–10^{1} km) (Fujita 1978, 1981b; McCarthy et al. 1982; Fujita and Wakimoto 1981; Wakimoto and Bringi 1988; AW91). Doppler radars employed in these studies alleviated the coarse nature of the observing networks to a degree, but often could not sample winds near the surface (especially at long distances). Peak horizontal wind velocities in downburst simulations (Chay et al. 2006; Kim and Hangan 2007; Mason et al. 2009; Orf et al. 2012) occurred within the lowest 100 m of the atmosphere, and observational studies have found peak velocities between 50 and 200 m above ground level (AGL) (Fujita and Wakimoto 1981; Gunter and Schroeder 2015; Canepa et al. 2020), well below the scanning capabilities of most operational radars except at very close ranges. As a result, downbursts previously classified as subsevere may have in fact contained small wind swaths exceeding NWS severe wind criteria.

These sampling problems persist today and have not been alleviated by modern observing networks. Table 1 gives the average station spacing of several in situ observing networks across the country. Most mesoscale networks have an average station spacing $O(30)$ km, which achieves the recommended network density for capturing most mesoscale phenomena (Dabberdt et al. 2005). However, these scales are likely insufficient to reliably capture storm-scale phenomena such as the peak winds of a downburst, and some stations may suffer from sheltering effects, resulting in unrepresentative wind measurements (Cook 2022). Similarly, the modern WSR-88D network is likely too coarse to adequately sample near-surface wind speeds beyond approximately 10 km. These deficiencies, combined with human observer tendencies to overestimate wind speeds (Adgas et al. 2012; Miller et al. 2016a; Edwards et al. 2018) and the potential for wind damage due to subsevere winds (Frelich and Ostuno 2012; Miller et al. 2016b), likely perpetuate the misclassification of severe downbursts and maintain the challenge of anticipating such events with substantial lead time and minimal false alarm.

Better understanding the spatial and temporal distribution of near-surface wind speeds and the probability of observing the peak wind speed with modern mesoscale observing networks may help forecasters reframe their assessment of convective environments, help determine the relative frequency of severe versus subsevere winds in damaging downburst events, and provide better guidelines for developing forecasting tools and techniques. These benefits are especially pertinent to forecasting wet downbursts across the southeast, which experiences a high frequency of WFTs conducive for wet downbursts (Miller and Mote 2017b) and has well-documented vulnerabilities to natural hazards (e.g., Emrich and Cutter 2011; Strader and Ashley 2018), but may provide utility for other regions that experience wet downbursts (Romanic et al. 2022). Furthermore, such information may be beneficial to the strategies and techniques of SVR warning issuance. This study will attempt to bolster this effort by achieving the following goals through a series of idealized high-resolution cloud model simulations:

- Describe the spatial and temporal distribution of downburst wind speeds in WFT environments associated with a damaging wind event, including the frequency of severe winds.

- Quantify the probability that a modern mesoscale surface observing network will sample winds reaching or exceeding severe thresholds given a severe downburst.

2. Methodology

a. *Model selection and configuration*

High-resolution numerical models have long been utilized to simulate both dry and wet downbursts. Many early studies used a cooling function to force negatively buoyant air parcels to the surface to replicate the surface outflow patterns of observed downbursts (Proctor 1988, 1989; Orf et al. 1996; Orf and Anderson 1999; Anabor et al. 2011). More recently, the Bryan Cloud Model (hereafter CM1; Bryan and Fritsch 2002) has been used to simulate both dry and wet downbursts (Orf et al. 2012; Oreskovic et al. 2018; Schumacher et al. 2023). CM1 has been used extensively for simulating convection on very fine spatial scales (<1 km) (e.g., Lane and Sharman 2014; Coffer and Parker 2015; Markowski 2016; Parker 2017; Orf et al. 2017; Chandrakar et al. 2021; Hiris and Gallus 2021; among others), making it an ideal choice for analyzing surface wind distributions in high detail. An additional benefit of the CM1 is the ability to control model settings across a series of simulations initialized from a variety of initial conditions. Running a series of simulations with a static model configuration (but differing initial conditions) of the same atmospheric phenomenon can lead to insightful statistics. One such example is Coffer et al. (2017), which examined tornadogenesis probabilities from a statistical perspective utilizing 30 unique CM1 simulations of tornadic and nontornadic supercells. To date, no studies have attempted to examine the statistical distribution of surface winds from WFTs using output from multiple high-resolution simulations in a manner similar to the Coffer et al. (2017) study.

This study utilizes CM1 Release 20, version 3 (https://github.com/george-bryan/CM1/blob/main/CHANGES), with an 80 km × 80 km horizontal grid at a grid spacing of 0.1 km. The model depth is set at 15 km and utilizes 84 vertical levels. Vertical grid spacing is held constant at 0.1 km below 2 km, stretched between 2 and 9 km, and held constant at 0.25 km from 9 to 15 km. CM1 utilizes a staggered velocity grid to help maintain numeric stability and preserve accuracy (Armfield 1991). Consequently, the use of 100-m vertical grid spacing below 2 km places the lowest model level at 50 m AGL, though diagnosed 10-m wind and 2-m temperature and moisture fields are output as well. A 1-s time step is used with model data output every 60 s. Each simulated storm is initiated in a horizontally homogeneous environment (determined by an input environmental sounding) via a single warm bubble with a positive 2-K thermal perturbation. The physical dimensions and starting location of the warm bubble are held constant between each simulation with a horizontal width of 10 km, vertical depth of 1.5 km, and starting vertical location of 0.5 km at the center of the model domain. This warm-bubble configuration was selected to replicate near-surface-based convective initiation and to maximize the number of successful simulations based on iterative testing, as done in previous large-eddy simulations of downbursts (Straka and Anderson 1993; Orf et al. 2012). For this study, the Morrison double-moment scheme (Morrison et al. 2005) is used since it accounts for both the mixing ratio and number concentration of rain, snow, graupel, and hail—all of which are important for resolving hydrometeor drag and the evaporative cooling processes that help drive the negatively buoyant downdraft (Wakimoto 1985; Wakimoto and Bringi 1988; Lee et al. 1992; Atlas et al. 2004). This microphysics scheme was used in the Orf et al. (2012) CM1 study of dry microbursts and yielded realistic results. Additional model configuration settings are outlined in Table 2 and are held constant between each simulation.

TABLE 2. Additional CM1 settings.

Horizontal advection scheme	Sixth order
Vertical advection scheme	Fifth order
Lower boundary condition	Semislip
Diffusion scheme	Sixth order
Subgrid turbulence	Deardorff TKE scheme (Deardorff 1980)
Lateral boundary conditions	Open radiative
Upper boundary condition	Free slip
Radiation scheme	None
Surface layer scheme	MM5 similarity theory
Land-use type	Low-intensity residential

The cold pools of observed WFTs are typically O(10–100) km in diameter with embedded burst swaths O(100) m (Fujita 1978, 1981b; Wilson et al. 1984; Caracena and Maier 1987; Proctor 1994). The 80 km × 80 km domain was selected in order to capture the peak velocities associated with the embedded burst swaths (rather than the evolution of the cold pool itself) while conserving computational time and space. A brief sensitivity analysis was performed to investigate the impact of horizontal grid spacing on the resulting outflow. Four simulations were initialized with the same input sounding, but used horizontal grid spacing of 0.05, 0.1, 0.2, and 0.5 km. The maximum 50-m horizontal wind speed decreased as a function of grid spacing with reductions of 2.4%, 8.4%, and 12.8% associated with the 0.1-, 0.2-, and 0.5-km simulations, respectively. Wind speed coverage decreased logarithmically as a function of grid spacing at the 20 m s^{-1} threshold, but coverage at the 24 m s^{-1} threshold was comparable between the 0.05- and 0.1-km simulations (the 0.2- and 0.5-km simulations had maximum winds below this threshold).

Similarly, a brief sensitivity analysis was performed to assess the influence of vertical grid spacing on the simulated convection. Three simulations were run with 84 (i.e., the configuration outlined in Table 2), 140, and 150 vertical levels, all using a 100-m horizontal grid. The 140-level simulation featured 50-m vertical resolution below 1 km and 150-m resolution above 9 km (a stretched grid was used between 1 and 9 km). The 150-level simulation used a constant vertical grid spacing of 100 m through the entire profile. Maximum 50-m wind speeds for both the 140- and 150-level simulations were within 1.5 m s^{-1} of the standard 84-level simulation, showing little sensitivity to vertical resolution. Interestingly, areal

coverage of 50-m winds at or above 24.0 m s^{-1} decreased by 25% in the 150-level simulation, with more substantial reductions (70%) found in the 140-level simulation. Qualitatively, the overall structure and evolution of the convective cell itself and its precipitation footprint were similar. Closer inspection of vertical velocity fields within the lowest 0.5 km reveals that these areal coverage differences are likely attributable to the intensity and size of the initial downdraft (the 140-level simulation produced a radially smaller downdraft with weaker downward velocity compared to the 84- and 150-level simulations).

These sensitivities to both horizontal and vertical grid spacings are not surprising based on the work of Proctor (1988) and Bryan et al. (2003), who found similar variations with grid spacings O(0.01–1) km. While realistic downbursts have been generated in previous studies using a 0.5-km grid resolution (Straka and Anderson 1993), the 0.1-km horizontal and vertical (below 2 km) grid spacings were chosen for this study as a deliberate compromise between sufficient resolution to capture the peak winds of most downburst events and saving computational time and storage space, which were practical limitations given the large datasets associated with this study. This horizontal grid spacing is similar to the grid spacing used by Schumacher et al. (2023) (0.125 km), which produced a realistic severe macroburst, and meets the recommendation of Bryan et al. (2003) who advocate for at least 0.1-km grid spacing for properly resolving the turbulent structures within convective clouds. However, the model domain and sensitivity tests indicate that this configuration may be too small to capture large outflows (>80 km in diameter) and/or too coarse to accurately resolve very fine-scale burst swaths (<0.2 km in diameter). Further implications are discussed in the summary and discussion.

Furthermore, it is acknowledged that the initial starting height and thermal perturbation of the warm bubble may not be optimal to produce the strongest possible convection for a given environment. However, the warm-bubble properties are held constant between simulations to minimize the degrees of freedom introduced into the study. A brief exploration into the sensitivity of the warm-bubble thermal perturbation on the resultant downburst was investigated through a series of five simulations roughly following the methodology of Brooks (1992). While some variability in peak wind coverage and intensity was noted as the thermal perturbation increased from 2 to 6 K (not shown), the variability of the resultant convection/downburst was considered sufficiently small to apply the default 2-K warm-bubble perturbation across all simulations.

It is also acknowledged that this experimental design will most closely simulate weakly forced, single-cell convection that is described well by Byers and Braham (1948) and Miller and Mote (2017a), which likely accounts for only a subset of all wet downburst events. However, this convective mode is relatively common across the southeastern United States during the summer months (Miller and Mote 2017b) and is known to cause the strong-to-severe wet downbursts that are the focus of this study (Caracena and Maier 1987; Kingsmill and Wakimoto 1991; Smith et al. 2013).

b. CM1 input sounding filtering and selection

Rather than focusing on individual convective events, this study aims to examine damaging WFT environments in a holistic sense by randomly selecting input soundings from a large sample of candidate environments. This large sample of environments was generated by first collecting 49 181 local storm reports (LSRs) that exclusively featured wind damage from the National Oceanic and Atmospheric Administration (NOAA) Storm Data database during the period 1 January 2018–31 August 2021. Nonmeteorological biases and artifacts associated with the Storm Data wind LSR dataset have been well documented (Weiss et al. 2002; Doswell et al. 2005; Edwards et al. 2018) and include LSR practices and methods that vary by region across the United States as well as unnaturally high frequencies of wind estimates ending in "0" or "5." However, this dataset is one of the most comprehensive collections of wind impacts currently available. The period 1 January 2018–31 August 2021 was chosen to reduce the potential influence of biases noted by Weiss et al. (2002) and Doswell et al. (2005) while still collecting a large sample of reports. Since these LSRs are not associated with measured wind speeds, it is likely that this sample consists of wind damage caused by both severe and subsevere wind speeds (Tirone et al. 2024).

For each report, a nearest grid hour and nearest grid point were assigned from the RUC/RAP-based (Benjamin et al. 2004), hourly, 40-km Storm Prediction Center (SPC) surface objective analysis (sfcOA; Bothwell et al. 2002). At each point and hour, most unstable convective available potential energy (MUCAPE) and effective bulk wind difference (EBWD) were recorded as measures of buoyancy and deep-layer wind shear. Composite environmental soundings derived from a climatology of WFTs in Miller and Mote (2017b) generally feature 0–6-km bulk wind difference (BWD) values < 10 m s^{-1} (19.4 kt), and Thompson et al. (2007) found that an EBWD value of 12 m s^{-1} (23.3 kt) discriminated between the 75th and 25th percentiles of all nonsupercellular and marginal supercell storms (respectively) in their study sample. Since the goal of this study is to simulate unorganized convection in environments similar to those described by Miller and Mote (2017b), the LSRs were filtered to retain only reports that featured MUCAPE values above 100 J kg^{-1} (to ensure that a buoyant parcel is present in the environment) and EBWD values below 10.2 m s^{-1} (20 kt). For each of the 13 069 reports that satisfied these criteria, an environmental profile of temperature, dewpoint, wind speed, and direction was collected at the corresponding grid point and hour with a vertical resolution of 25 mb from the surface to 100 mb (1 mb = 1 hPa). While the exact storm mode associated with each report is unknown, these candidate profiles represent environments associated with damaging wind events. Based on the results of Miller and Mote (2017b), this represents a relatively small (0.6%) subset of all WFTs.

Using environmental profiles from the sfcOA dataset has a couple of distinct advantages. The spatial and temporal resolution of the sfcOA dataset is considerably higher than the observed rawinsonde network and allows for data collection

closer to the time of the actual severe event compared to observation-based networks. This allows for better resolution of the diurnal heat maximum, which tends to correspond with the most frequent time of occurrence of downbursts (Wakimoto 1985; AW91). Additionally, sfcOA profiles have been utilized extensively in previous work and their potential limitations and biases have been well documented. For example, Thompson et al. (2003) and Coniglio (2012) documented surface-based CAPE (SBCAPE) [mixed-layer CAPE (MLCAPE)] errors on the order of −300 to 500 (−200 to 250) J kg^{-1} as well as a 1–2 m s^{-1} high bias in low-level winds compared to observed soundings. However, Coniglio (2012) acknowledged that the sfcOA profiles improved upon 1-h RUC forecast soundings due to the incorporation of surface observations in the hourly analyses. More recently, Coniglio and Jewell (2022) found a 2–4 m s^{-1} low bias in near-ground winds when comparing sfcOA soundings to observed field study soundings but noted nearly unbiased dewpoint values near the surface with a slight dry bias above 1 km. Thermodynamic errors throughout the profile will propagate into other measures of convective potential, such as any buoyancy parameter. These errors could be detrimental when studying low-buoyancy environments where an error of a few 100 J kg^{-1} can influence a forecaster's interpretation of convective potential. As it will be shown later, the environments in this study generally feature high values of MUCAPE (over 1000 J kg^{-1}), so such errors will be less influential in the subsequent simulations and analyses. Previous work on downbursts suggests that outflow generation is primarily a function of the thermodynamic properties of the environment rather than low-level kinematics. Hence, the small errors in the sfcOA wind profiles documented by prior studies (e.g., Coniglio and Jewell 2022) should not be overly detrimental.

One known source of error in this study involves the calculation of convective parameters as compared to known sfcOA values. A more thorough environmental assessment of each candidate profile was completed using the MetPy version 1.6 software (May et al. 2022). This meteorological analysis library utilizes slightly different methods for determining buoyancy metrics (such as MUCAPE) than the methodology employed by sfcOA (Hart and Korotky 1991). Similarly, as of version 1.6, MetPy does not offer a way to directly calculate the effective inflow layer or any related variables such as EBWD. A methodology for determining the effective inflow layer (and related variables) was custom written based on the definition of the effective layer found in Thompson et al. (2007). A comparison of the sfcOA EBWD values to the custom, sounding-derived EBWD values found a bias of 1.2 m s^{-1}, which was considered sufficiently small to not mischaracterize the nature of the convective environment. However, this did result in some profiles near the 20-kt sfcOA threshold being recalculated above the threshold.

Additional sfcOA profile limitations are highlighted by Thompson et al. (2012), who noted the tendency for convective storms to develop in the vicinity of baroclinic zones, which may lead to an unrepresentative sfcOA profile if the underlying RUC/RAP model inaccurately analyzes the position of the thermal gradient. Similarly, Potvin et al. (2010) focused on potential problems with choosing proximity soundings too close or too far from a target storm as a representation of the storm environment. In light of these concerns, it is acknowledged that creating a profile at the grid point and hour closest to the wind damage LSR does not necessarily guarantee a profile that perfectly represents the target convective environment. However, as with previous studies (Grams et al. 2012; Brotzge et al. 2013; Anderson-Frey et al. 2016; Brown et al. 2021), these concerns are mitigated by utilizing a large sample size such that errors in individual profiles should not have a significant impact on subsequent analyses. This assertion is supported below by comparing the environmental distribution of the candidate profiles to documented WFT environments.

The spatial distribution of candidate soundings (Fig. 1) reveals the highest concentration of reports across the mid-Atlantic, with decreasing density southwestward along the Appalachians into the southeastern United States. Candidate soundings become increasingly sparse west of the Mississippi River and into the High Plains and the southwestern United States, where thermodynamic profiles tend to favor dry downbursts (Wakimoto 1985). The LSR maximum across the mid-Atlantic region may be influenced to some degree by higher population density, but is more likely influenced by local Weather Forecast Office (WFO) LSR reporting practices (Weiss et al. 2002; Doswell et al. 2005) and higher forest density (i.e., more potential damage indicators) compared to other regions east of the Mississippi River (Woodall et al. 2006). This idea is consistent with the findings of Smith et al. (2013), who noted that the greatest concentration of wind LSRs shifted from the southern Appalachians to the central High Plains when only considering measured wind reports, implying that most wind reports east of the Mississippi River were associated with wind damage rather than measured severe wind speeds. Although not the maximum, high kernel density values are noted across the southern Appalachians and into the southeastern United States, which has been the focus of multiple previous wet downburst studies (Dodge et al. 1986; AW91; Miller and Mote 2017b) and compares well with the frequency of days with wind-damage-producing WFTs noted in Miller and Mote (2018; hereafter M18).

Although no geographic restrictions were placed on the locations of the candidate soundings, the goal of this study is to primarily focus on wet downbursts. Therefore, certain thermodynamic restrictions are required to filter out soundings that may be described as a dry downburst environment rather than a wet downburst environment. While no clear selection criteria emerge from previous studies, Wakimoto (1985) found that dry downbursts are typically associated with environments that feature a deep, well-mixed boundary layer (the prototypical "inverted-V" profile) with dry-adiabatic lapse rates between 9.0° and 10.0°C km^{-1} extending from the surface (where a shallow superadiabatic layer may be present) to the cloud base. Conversely, AW91 found that wet microburst environments tended to feature warmer cloud bases, lower midlevel lapse rates, and shallower subcloud layers with higher relative humidity compared to dry microburst environments. The climatological studies of Miller and Mote (2017b,

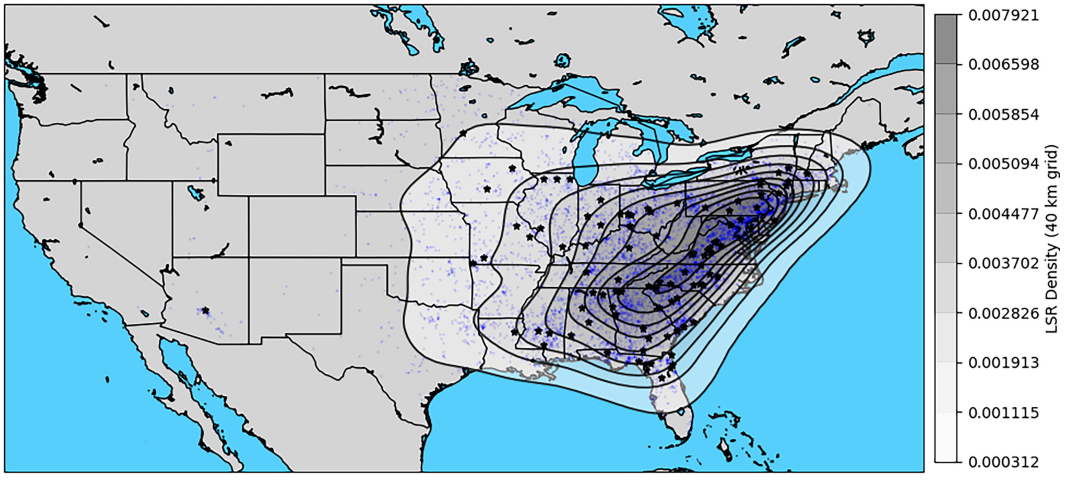

FIG. 1. The kernel density estimate (number of LSRs per square kilometer over a 40-km grid; fill) of all candidate wind damage LSRs (blue dots) during the period 1 Jan 2018–31 Aug 2021, as well as the locations of the CM1 initialization soundings for this study (black stars).

2018) more fully described environments associated with weakly forced thunderstorms and similarly found lower (mid)-tropospheric relative humidity values on the order of 75%–80% (50%–70%), as well as equivalent potential temperature (theta-e) deficits (the difference between the maximum theta-e value in the lowest 700 mb and the lowest theta-e value above 700 mb; AW91) between 20 and 30 K and MLCAPE values generally between 1000 and 2000 J kg^{-1}.

To create a dry/wet environmental filter, a mean profile of temperature and dewpoint was compiled from the 13 069 candidate soundings (not shown). This profile featured a surface to 3 km AGL lapse rate of 5.0°C km^{-1}—considerably less than the 9.0°–10.0°C km^{-1} lapse rates found by Wakimoto (1985). Furthermore, the surface to 850 mb (850–500 mb) mean relative humidity value was 66% (62%) with a theta-e deficit of 21.0 K and MLCAPE value of 1214 J kg^{-1}. These metrics more closely align with the characterization of a wet downburst environment outlined by AW91 and Miller and Mote (2017b, 2018), lending confidence that a considerable portion of the candidate soundings are likely wet downburst environments. Since the lower-tropospheric relative humidity profiles of dry and wet downburst environments tend to be dissimilar, a measure of low-level relative humidity was chosen to differentiate between "dry" and wet candidate soundings. More specifically, the standardized deviation (or *Z*-score) of the 0–3 km AGL mean relative humidity from each candidate sounding is computed against the same metric of the mean profile. This allows for an objective measure of how much the candidate deviates from the target environment. A *Z* score of ±2 was chosen as a cutoff to eliminate profiles that were too moist (likely due to convective contamination) or too dry to be considered a wet downburst environment. This eliminated 530 candidate soundings from consideration.

The remaining candidate soundings were randomly sampled without replacement to be used as the initializing sounding for a CM1 simulation. Each selected sounding was plotted and inspected for any overt errors prior to the simulation. A successful CM1 simulation was defined as a simulation in which convection was generated, the initial downburst occurred within the model domain, and numerical stability was maintained during the full 2-h model integration time. Some simulations featured outflow winds that spread beyond the model domain after the initial downburst. In such cases, it was subjectively determined whether the wind field within the domain was representative of the downburst as a whole. A general guideline was whether the maximum wind swath was captured within the model domain. If not, the simulation was omitted from further consideration. This method was chosen to expedite the simulation-generating process after tests using moving domains yielded only marginal improvements, largely due to convective outflow outpacing the mean storm motion used to determine the domain motion. Furthermore, simulations that began to autoconvect during the 2-h simulation time were omitted from the study; this was an infrequent occurrence associated with deeply mixed environments with no inhibition. Candidate soundings that were too close spatially (within 1° latitude or longitude) and temporally (same grid hour) to a previously successful CM1 simulation were not used. This process was repeated until 97 valid simulations were generated for analysis.

c. *Environmental distributions of input soundings*

Environmental distributions of the 12 539 candidate soundings and the 97 CM1 input soundings were compiled (Fig. 2) and compared to previously documented wet downburst environments to ensure that the target phenomena can be accurately simulated. The analyses of WFT environments by M18 provide useful metrics for comparison. For example, the interquartile ranges of MLCAPE (Fig. 2b), vertical totals (VTs; Fig. 2g), total totals (TTs; Fig. 2h), theta-e deficits (TEDs; Fig. 2i), and downdraft CAPE (DCAPE; Fig. 2j) fall within similar ranges as the "severe-wind-supporting" WFT events in M18. One caveat to consider is that the environmental climatology produced by M18 did not explicitly differentiate

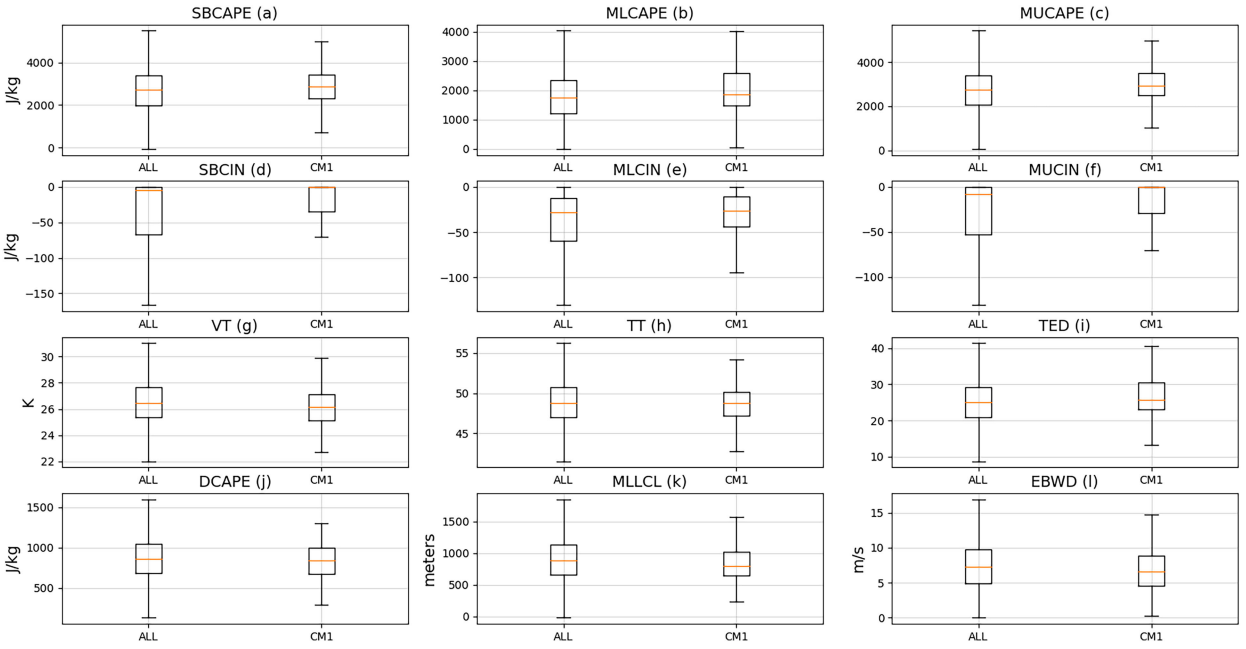

FIG. 2. A comparison of the environmental distributions between all CM1 candidate soundings (ALL; $N = 12\,539$) and the soundings used to initialize the CM1 simulations (CM1; $N = 97$), which are both subsets of the wind damage LSR dataset.

between downburst- and nondownburst-related damaging wind events. Nonetheless, the environments in this study appear to be consistent with the fact that the candidate profiles were all associated with wind damage of some form. The 25th percentile of theta-e deficits (Fig. 2i) is near (above) 20 K for the candidate profiles (CM1 initialization soundings), which indicates that at least 75% of the environments are above the 20-K criteria for a wet microburst environment proposed by AW91.

Additional environmental comparisons are made by generating a composite profile from the 97 CM1 initialization soundings (Fig. 3). This mean profile shares similarities with previously documented wet microburst profiles (Kingsmill and Wakimoto 1991; McCann 1994; Wheeler and Spratt 1995; Atlas et al. 2004) and the wet microburst model profile developed by AW91. One of the more important features of this mean sounding is the relatively shallow (below 800 mb) mixed-layer LCL height with a 0–3-km lapse rate of 7.4°C km^{-1} and layer-average relative humidity of 68%. This is in contrast with the deeper, drier boundary layers found in dry downburst environments that typically feature steeper low-level lapse rates (Wakimoto 1985; Wakimoto et al. 1994). Additionally, a mean EBWD value of 6.2 m s^{-1} (12 kt) suggests low potential for organized convection (i.e., supercells) based on Thompson et al. (2007), and the mean theta-e profile (not shown) is similar to previously documented wet downburst environments (Kingsmill and Wakimoto 1991; AW91; Wheeler and Spratt 1995). The 97 CM1 initialization soundings span the months of May through October with the majority (90%) of the soundings occurring during the summer months of June, July, and August. Temporally, the soundings ranged from 1400 to 0100 UTC, with 74% occurring within the 1800–2200 UTC period. These temporal statistics fall within the period of peak diurnal heating for the eastern CONUS summer and are comparable to the most common downburst occurrence times documented by AW91 (1500–1600 CDT). These comparisons lend confidence that the environmental distributions characterized by Figs. 2 and 3 and the CM1 input soundings are representative of wet downburst environments.

3. CM1 simulation results

a. CM1 simulations compared with reality

Prior to drawing statistical inferences from the results of the 97 simulations, a qualitative assessment was performed to ensure that the simulated downbursts are reasonably representative of reality. Convection generated by each of the CM1 simulations generally adheres to the definition of "weakly forced thunderstorms" or "air mass thunderstorms" established within the meteorological community (Miller and Mote 2017a). Convection in all simulations produced rainfall at the surface with an average maximum rainfall amount of 2.56 cm (1.01 in.). All but two simulations resulted in rainfall amounts over 0.25 cm (0.1 in.), and four simulations produced rainfall amounts over 5.08 cm (2.0 in.). Time-series analyses of both composite reflectivity and maximum vertical velocity (not shown) indicate that nearly all simulated storms reached peak intensity within the first 3600 s of model integration, followed by a gradual weakening as the convective cold pool expanded. One example of this process is given in Fig. 4, wherein the initial warm-bubble-driven updraft reaches peak intensity around 1800 s. This is followed by a rapid intensification and expansion of the cold pool, which undercuts the initial cell and initiates the weakening trend. Attempts at reintensification of

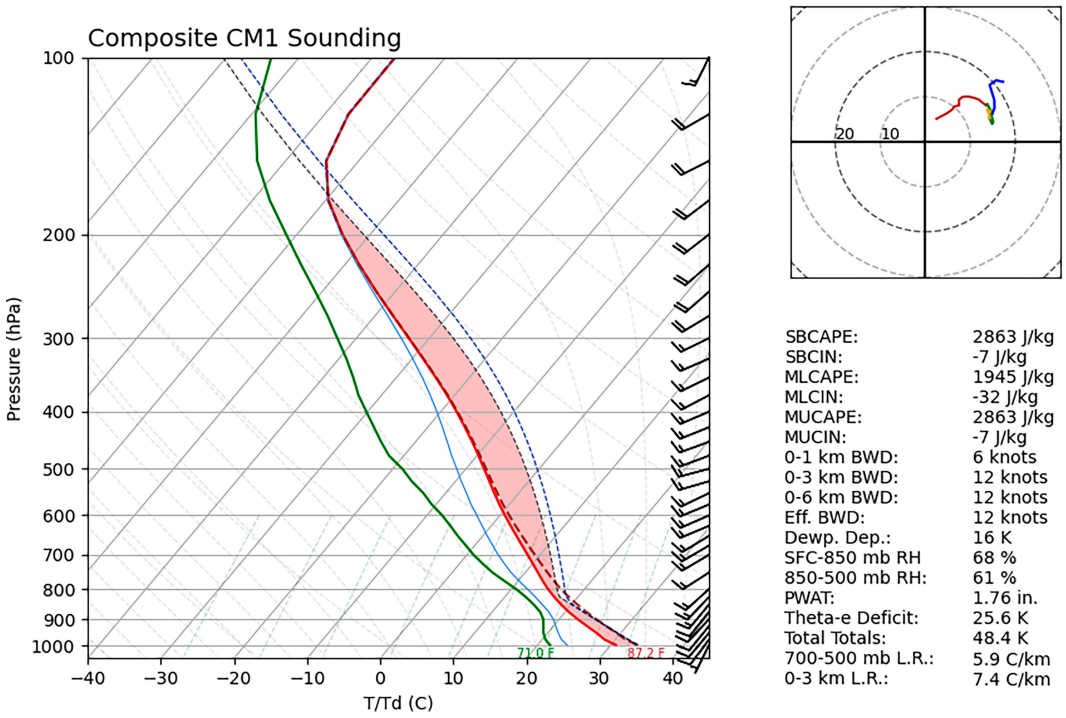

FIG. 3. A mean sounding compiled from the 97 CM1 input soundings. The temperature and dewpoint profiles are denoted by the red and green lines, respectively; virtual temperature and wet-bulb temperature by the dashed dark red and light blue lines, respectively; and surface-based and mixed-layer parcel profiles by the dashed light blue and dashed black lines, respectively, with MLCAPE filled in red. Wind barbs and hodograph winds are in units of knots.

the convective cell are noted between 3600 and 5400 s on the southern periphery of the cold pool as parcels are lifted along the outflow boundary. However, the absence of vertical wind shear and diminishing ascent along the weakening outflow boundary prohibit storm maintenance. This evolution is common for weakly forced thunderstorms based on past literature (Byers and Braham 1948; Markowski and Richardson 2010; Miller and Mote 2017a) and is observed in weakly sheared environments in nature. One such example is given in Fig. 4d, which depicts the evolution of a weakly forced thunderstorm along the Mississippi/Tennessee border on 12 July 2018.

Closer inspection of the CM1 simulations reveals further similarities with previously documented downburst characteristics. For instance, the outflow emanating from one of the strongest simulated downbursts (which featured peak near-surface wind speeds above 30 m s^{-1}) displays asymmetrical characteristics, with the strongest winds found on the downwind side of the downburst relative to the environmental wind field (Fig. 5a). This pattern is identical to the numerical results of Orf and Anderson (1999) and Mason et al. (2010), the experimental results of Romanic and Hangan (2020), and observations by Kingsmill and Wakimoto (1991) and Caracena and Maier (1987). A cross-sectional analysis across the cold pool reveals a classic rotor on the upwind edge (e.g., Fig. 5b), a well-documented phenomenon in both observed and simulated microburst and downburst studies (Rinehart and Isaminger 1986; Hjelmfelt 1988; Proctor 1988; Kingsmill and Wakimoto 1991; Anabor et al. 2011). A less coherent rotor is noted in the potential temperature perturbation field on the downwind side of the gust front, and while not formally described or investigated, it was qualitatively noted that the symmetry of the rotor around the cold pool varied as a function of the low-level wind profile. However, this is expected based on the results of Mason et al. (2010). In the simulation depicted in Fig. 5, the peak radial velocities were associated with the passage of the downwind gust front and attendant rotor, though it was not investigated whether this was the case for all simulations.

Multiple numerical simulations of downbursts (e.g., Chay et al. 2006; Kim and Hangan 2007; Mason et al. 2009, 2010; Vermeire et al. 2011; Orf et al. 2012; Oreskovic et al. 2018) have documented the shallow nature of the outflow winds with peak radial velocities generally occurring within the lowest 100 m AGL. Sampling the vertical wind profile from within the gust front reveals a similar structure; the strongest winds were found at 50 m AGL, quickly decreasing to below 10 m s^{-1} above 250 m (Fig. 5c). Similar vertical wind profiles within the gust front were observed in the other 96 simulations, with peak radial velocities found at either 50 or 100 m AGL. A time series of 10- and 50-m wind speeds (Fig. 5d) shows the rapid onset of outflow winds associated with the passage of the gust front, followed by additional outflow surges of diminishing amplitude in a fashion similar to previous observational (Wakimoto 1985; Wakimoto et al. 1994; Wheeler and Spratt 1995) and simulated studies (Orf and Anderson 1999; Kim and Hangan 2007; Vermeire et al. 2011;

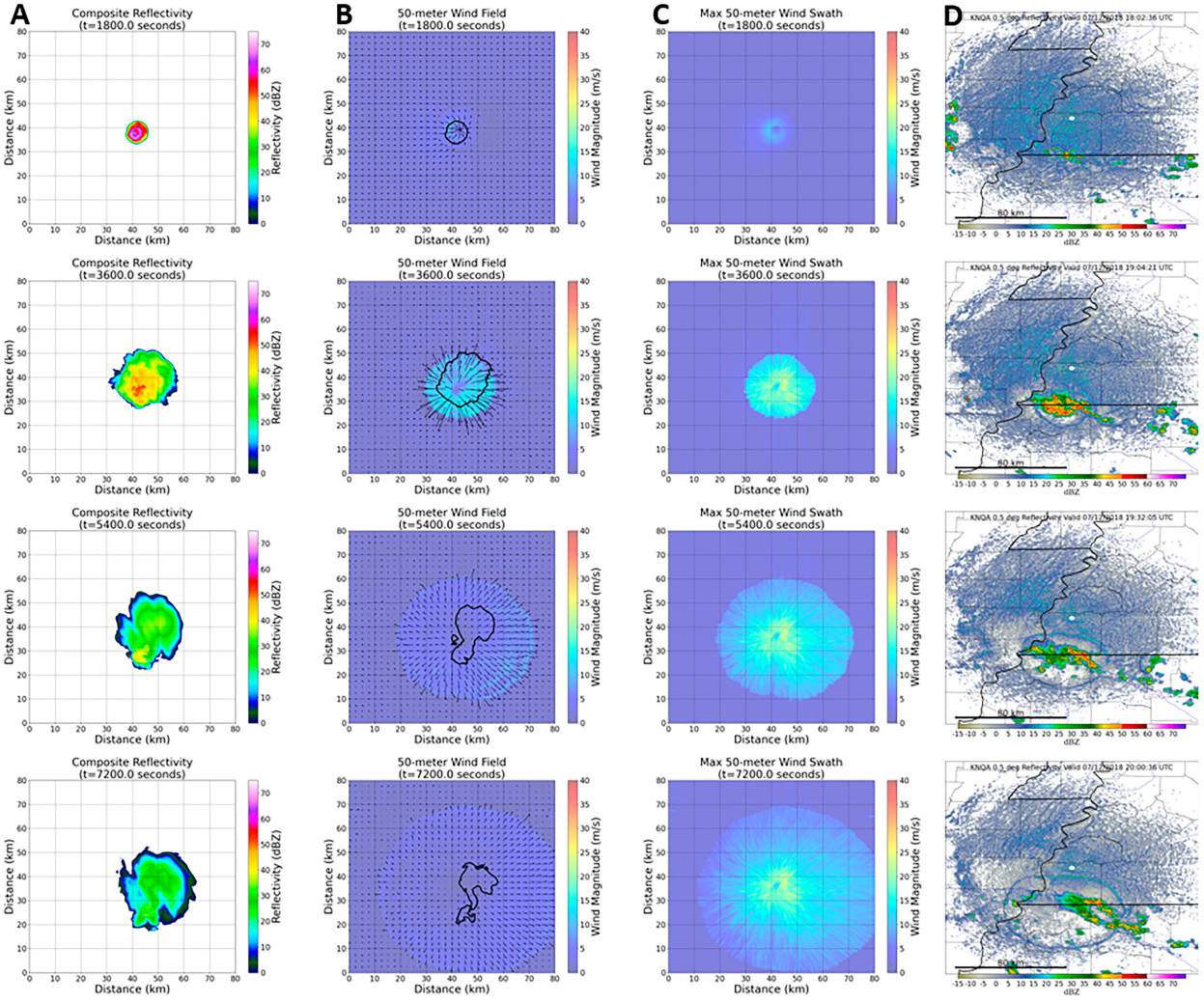

FIG. 4. The life cycle of a simulated air mass thunderstorm from CM1 and a comparison to an observed downburst on 12 Jul 2018. Each column shows (a) composite reflectivity; (b) instantaneous 50-m horizontal wind magnitude (fill), vectors (arrows), and 25-dBZ contour (black line); (c) accumulated 50-m horizontal wind magnitude (fill) at simulation times 1800, 3600, 5400, and 7200 s (shown from top to bottom); and (d) KNQA (Memphis, Tennessee) 0.5° reflectivity imagery valid at times 1802, 1904, 1932, and 2008 UTC (shown from top to bottom).

Orf et al. 2012; Romanic and Hangan 2020). These results suggest that the simulated surface wind fields can be considered representative of actual downburst wind fields.

b. 50- versus 10-m winds

CM1 maintains a record of the maximum horizontal wind speed at the lowest horizontal velocity level at every time step (1 s) during model integration. This record is output at every output time step (60 s) as a "maximum wind swath" grid. As previously mentioned, using a 100-m vertical spacing below 2 km AGL places the lowest model level at 50 m AGL. Instantaneous surface diagnostic variables are also generated at every output time step, which includes U and V winds at 10 m AGL. A maximum 10-m wind speed grid can be created by recording the maximum 10-m wind magnitude at each grid point across all output time steps, which allows for a comparison of the 10- and 50-m wind speed distributions. Across all simulations, the 10-m winds were weaker than the 50-m winds, with an average 50:10-m wind speed ratio of 1.97. This result is not surprising and has been reported in both high-resolution numerical studies of downbursts (e.g., Orf et al. 2012) and observational studies of thunderstorm outflows (Gunter and Schroeder 2015).

Although this ratio is reasonably comparable to observed thunderstorm gust ratios (Choi and Hidayat 2002; Shu et al. 2015; Mohr et al. 2017), there are limitations to utilizing maximum 10-m wind speeds. Unlike the 50-m maximum wind swath grids, the diagnostic surface variables are instantaneous measures at the output time step (60 s) rather than a maximum or mean value derived from each model time step (1 s). Consequently, the maximum 10-m wind speed may occur between output time steps and go undocumented. This manifests as a "ripple" effect in the maximum 10-m wind fields and can easily be observed by comparing the 50- and 10-m

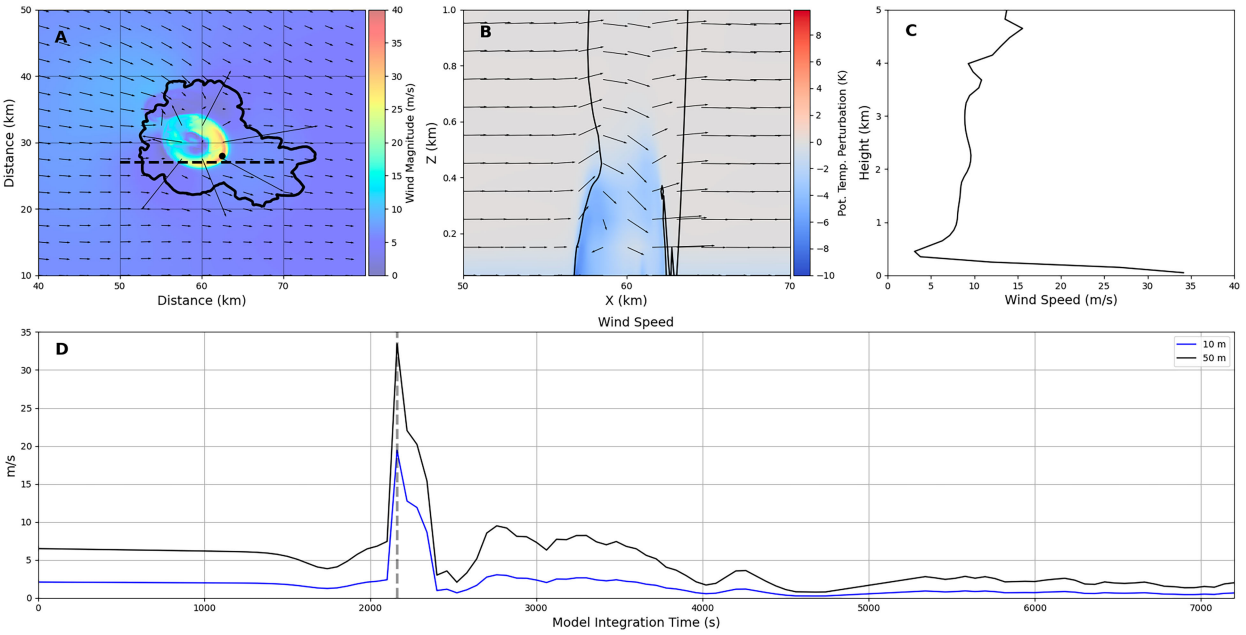

FIG. 5. (a) Instantaneous 50-m wind magnitude (fill), velocity vectors (arrows), and 25-dBZ contour (black line) of a downburst simulation at model integration time 2220 s. The black dashed line denotes (b) the location of the cross-sectional analysis of potential temperature perturbation (fill), the 25-dBZ reflectivity contour (black), and velocity vectors (arrows) below 1 km, while the black dot denotes (c) the location of the concurrent vertical wind profile and (d) the location of the 10- and 50-m wind speed time series. Note that the domain in (a) is zoomed to focus on the outflow wind field.

maximum wind swath fields at the end of each model simulation; one such example is given in Fig. 6.

Additionally, Markowski and Bryan (2016) demonstrated that an LES simulation using a semislip lower boundary condition that does not invoke turbulent eddies during model initialization may suffer from unrealistically high surface friction, resulting in muted wind speeds near the ground. This criterion applies to this study, suggesting that the 10-m winds may be unrealistically low. Comparisons with the vertical wind speed profiles observed by Gunter and Schroeder (2015) lend credence to this idea. The 50:10-m wind speed ratios in the Gunter and Schroeder (2015) analyses appear lower than the 1.97 ratio found here. For these reasons, the 50-m winds are preferable for analysis over the 10-m winds and are interpreted as a proxy for surface wind gusts rather than sustained wind speeds.

Observational studies lend support to this method, as Gunter and Schroeder (2015) documented a few instances of 10-m winds matching 50-m wind speeds, and Canepa et al. (2020) found instances of similar thunderstorm outflow wind speeds at 20 and 120 m AGL. Such an interpretation is not without precedent in the modeling and wind engineering communities. For

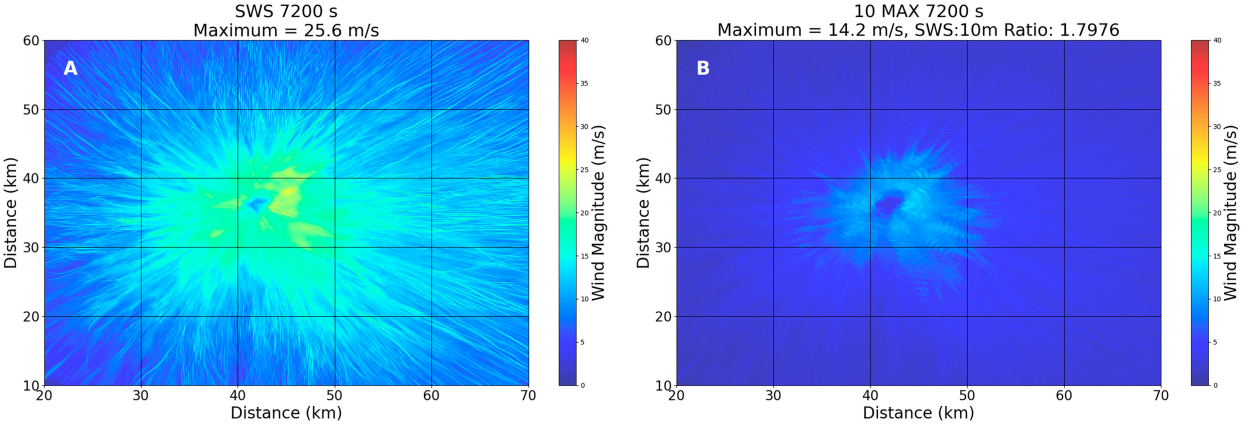

FIG. 6. An example of (a) the 50-m maximum wind swath compared to (b) the 10-m maximum wind swath valid at the end of the simulation (7200 s). The domain is zoomed to focus on the region of strongest 10- and 50-m winds.

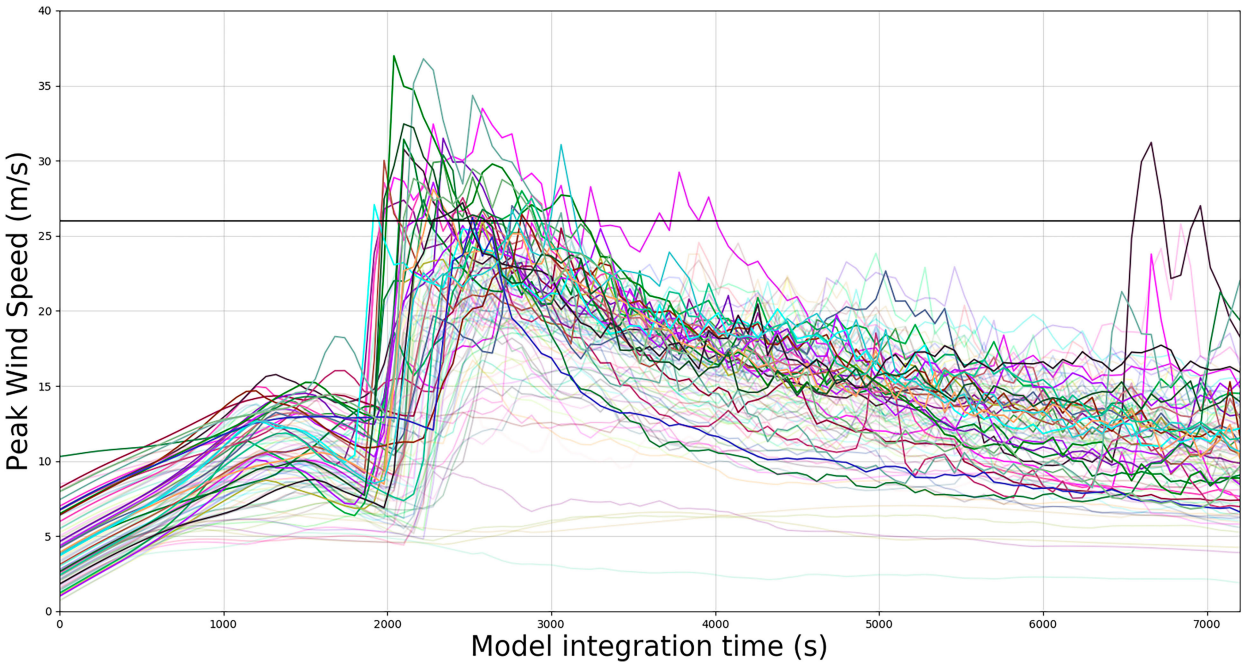

FIG. 7. A time series of the domain maximum 50-m wind speed for each simulation. Bold lines indicate simulations that reached severe wind criteria.

example, the Warn-on-Forecast System (WoFS) uses 80-m winds as a proxy for 10-m wind gusts (Dahl et al. 2022), and Oreskovic et al. (2018) analyzed 50-m gusts to assess the peak winds experienced by structures and transmission towers. Hereafter, all wind speed analyses will utilize the 50-m wind field (which will be referred to as "near-surface" winds) and should be interpreted as 10-m gusts rather than sustained winds.

c. Temporal duration of winds

At each time step, the maximum 50-m wind speed within the model domain is recorded, resulting in a history of the peak near-surface winds over the course of each simulation (Fig. 7). In general, these time series follow the documented evolution of downburst wind fields, with a clear ramp-up period as the initial downdraft reaches the surface, followed by a gradual dissipation period (Romanic and Hangan 2020). Thirty-four simulations reached or exceeded the NWS SVR threshold, and nearly all simulations experienced their peak wind velocity roughly within 1000 s after the initial downburst reached the surface. Two simulations experienced secondary peaks later in the run as a result of convection initiating along the initial outflow boundary. The average (though not necessarily continuous) duration of winds above 26 m s^{-1} at any point in the domain was 5.2 min, with a minimum of 1 min (the smallest output time step) and a maximum duration of 17 min. This average duration of severe winds compares well with the duration of maximum surface winds in other numerical studies of microbursts (Orf and Anderson 1999; Orf et al. 2012) as well as some observed cases (Wilson et al. 1984). The total duration of winds exceeding 20 m s^{-1} is much longer, lasting on average 25 min; likewise, winds exceeding lower thresholds persisted for even longer durations.

d. Severe downburst frequency

Spatial analyses of the downburst wind fields are conducted using the final 50-m maximum wind swath field valid at the end of each simulation. To focus the analyses on the downbursts themselves, it was desirable to isolate the downburst wind field from the surrounding environmental wind field. Environmental winds were removed from each maximum wind swath field by masking wind speeds below the median value of the field. Given the weak environmental winds (generally $<$10.0 m s^{-1}), this effectively isolated the downburst wind fields as desired. The frequency at which wind thresholds were reached at any grid point across the 97 simulations can then be determined.

Such frequencies are given in Fig. 8 for an assortment of wind speeds of 10 m s^{-1} and higher. The inverse relationship between wind magnitude and frequency of occurrence is worth noting. This trend follows previous studies of severe wind, such as Edwards et al. (2018), which found a similar inverse relationship between wind magnitude and LSR frequency. A similar relationship was found by Lombardo and Zickar (2019) who noted a positive relationship between yearly return intervals with increasing wind speed (i.e., stronger wind speeds had smaller annual probabilities of occurrence). Also noteworthy is the fact that 80% of the simulated downbursts featured winds at or above 20 m s^{-1}, and over half (53%) produced winds at or above 24 m s^{-1}. While subsevere by NWS criteria, such wind speeds have been documented to inflict tree damage (Frelich and Ostuno 2012).

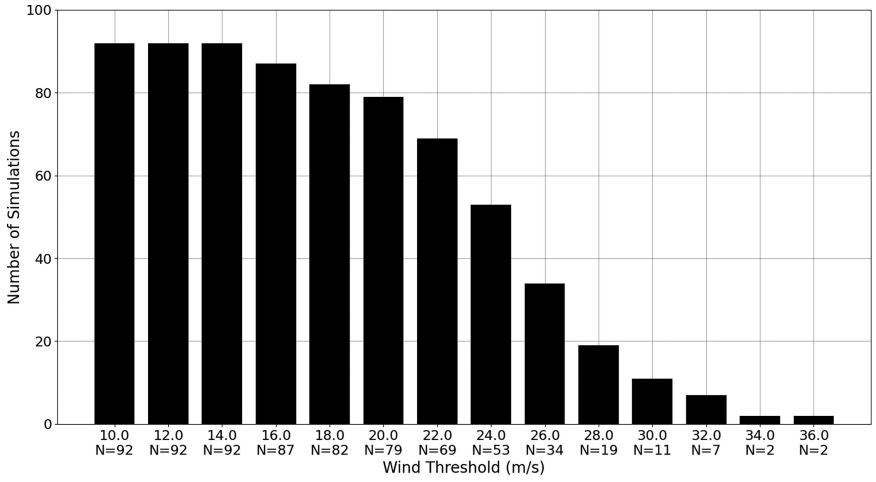

FIG. 8. Frequency counts depicting the number of simulations that reached or exceeded a given wind threshold.

Thirty-five percent of the simulated downbursts produced winds at or above severe criteria, the occurrence of which corroborates previous observational studies with in situ measurements of severe winds from poorly organized, short-lived convection (e.g., AW91).

Downburst wind speeds can be aggregated across all simulations to create a probability density function (PDF) that describes the likelihood of observing a wind speed range at any location on the grid. Such a PDF is given in Fig. 9 and takes on the shape of a gamma distribution, which has been documented in other convective wind studies (Mohr et al. 2017; Edwards et al. 2018). Damaging wind speeds reside well within the tail of this distribution. For example, a wind speed of 15 m s^{-1} is in the 90th percentile of the distribution, while a wind speed of 21 m s^{-1} is at the 99th percentile. Likewise, NWS severe wind criteria (26 m s^{-1}) have a percentile rank of 99.9%. Although severe winds were recorded from at least one grid point in 35% of the simulations, this percentile rank indicates that the probability of observing such wind at any given point in the downburst wind field is very small. The peak wind speed from any downburst is 37 m s^{-1} and only occurred in a single simulation. However, this result compares well to maximum wind gusts in observed microbursts (Caracena and Maier 1987) as well as previous numerical simulations of wet microbursts (Anabor et al. 2011). The maximum of the wind speed distribution may also hint at the inherent intensity limitation of wet downbursts, though this hypothesis is not explicitly tested here.

e. *Spatial coverage of winds*

To further illustrate the low probability of observing severe winds, the spatial coverage of wind speeds reaching or exceeding set thresholds was assessed (Fig. 10). The areal coverage of a given wind threshold was determined by first assuming that the area surrounding each grid point can be approximated as a square with the same dimensions as the horizontal grid spacing (in this case, 0.1 km × 0.1 km). This methodology overapproximates the domain area slightly by

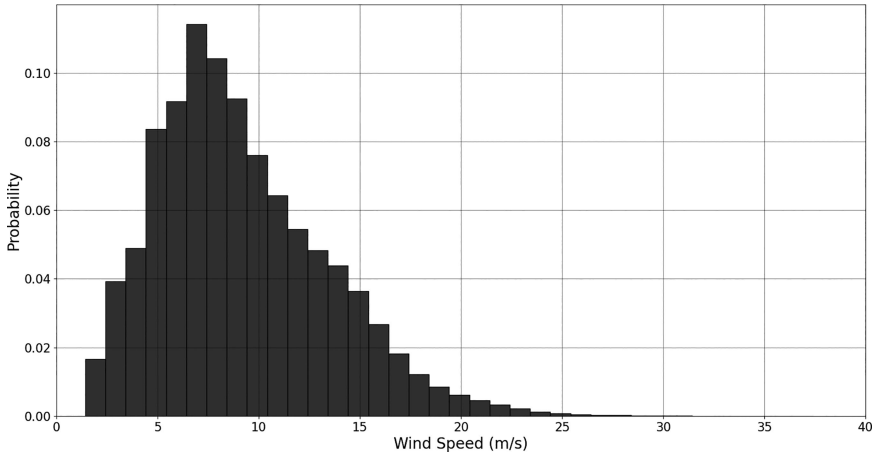

FIG. 9. PDF of 50-m downburst wind speeds across all simulations.

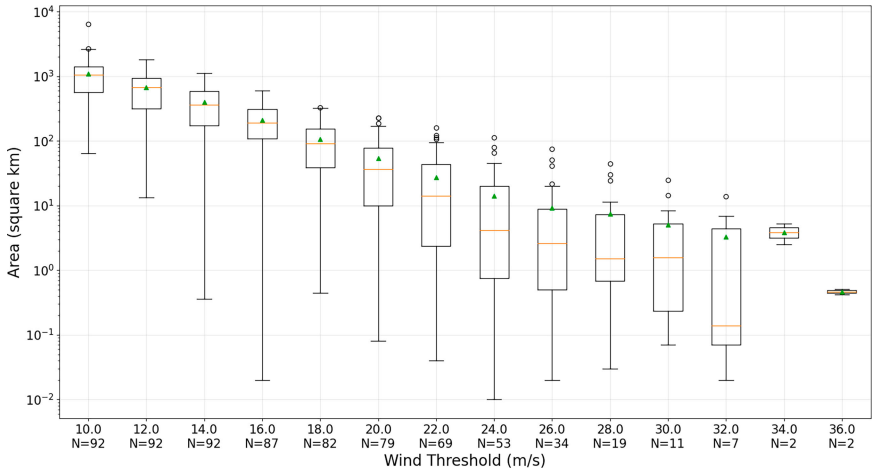

FIG. 10. Distribution of wind magnitude coverage (km^2) by wind threshold ($m\ s^{-1}$). The median of each distribution is denoted by the orange bars; the mean is denoted by green triangles.

assuming grid points on the edge of the domain have the same area as grid points inside of the domain, but this error was found to be very small. By using simulations that feature outflows that exit the model domain, the spatial coverages of some wind speeds (mainly lower wind speeds away from the primary burst swaths) may be underestimated to some degree.

Across all simulations, the spatial coverage decreased as a function of the wind speed threshold, which generally follows the same trend outlined in Fujita and Wakimoto (1981). The aggregate coverage of winds reaching or exceeding the 10–16 m s^{-1} thresholds is comparable and is $O(10^2$–$10^3)$ km^2. Increasing the threshold to 18–24 m s^{-1} decreases the coverage by roughly one order of magnitude, and the median coverage falls further to 10^0 km^2 when considering the 26 m s^{-1} threshold. Of the 34 simulations with 10-m wind speeds over severe criteria, only eight (23%) exhibited swaths of severe winds $> 10^1$ km^2. This result supports the implications of Fig. 9, suggesting that the probability of severe winds impacting any damage indicators (such as trees, power lines, and/or buildings) is considerably reduced compared to lower wind speed thresholds given the very small spatial footprint. Coverage of 30+ m s^{-1} winds continues the downward trend, but sample sizes above this threshold fall off considerably to 11 simulations or less, which limits confidence in drawing further conclusions regarding spatial trends.

Such small swaths of severe winds tie directly into the operational warning challenge. Drawing from a collection of SVR warnings from across the contiguous United States, Harrison and Karstens (2017) found that the national average SVR warning area was 1802 km^2. A severe wind swath with an area $O(10^1)$ km^2 would verify only 0.9% of this warning area, while the maximum severe wind coverage (10^2 km^2) would verify 9.2%. Conversely, 99.91% and 90.8% of the warning area, respectively, would experience a false alarm. These metrics are intended for illustrative purposes rather than a robust quantification of SVR warning performance in WFT events, but they help convey the challenge of issuing SVR warnings for WFT downbursts and highlight the potential for considerable false alarm area.

f. *Environmental predictors*

Although not the primary focus of this paper, environmental parameters that may discriminate between severe and subsevere downbursts are briefly explored here given the potential applicability to operational forecasts. Figure 11 gives the same environmental parameters as Fig. 2 with samples parsed between CM1 initialization soundings that resulted in severe downburst winds versus subsevere downburst winds. As found by M18 and Romanic et al. (2022), traditional metrics for severe thunderstorm potential such as MLCAPE and deep-layer wind shear (e.g., EBWD) were poor discriminators between severe and subsevere environments. Some differentiation is noted in TTs (Fig. 11h), TEDs (Fig. 11i), and mixed-layer LCL (MLLCL) (Fig. 11k) between severe and subsevere classes, which supports previous work on environmental discrimination (M18; AW91; Romanic et al. 2022). However, the overlap in the interquartile ranges between these variables suggests that using set thresholds for either variable may provide limited utility for operational forecasts.

Interestingly, surface-based convective inhibition (SBCIN) and most unstable convective inhibition (MUCIN) (Figs. 11d,f, respectively) both appear to show some discrimination between the two classes. (It is worth noting that these distributions are similar owing to the fact that most profiles were sampled during the mid- to late afternoon hours when the surface-based parcel is the most unstable parcel.) One possible explanation for this result is that convective inhibition could reduce updraft intensity of surface-based/most unstable parcels, possibly resulting in less hydrometeor production and subsequently less precipitation drag and evaporative cooling of the downdraft, though exploring this theory is beyond the scope of this study. However, the fact that the median values of SBCIN and MUCIN for both classes are zero suggests that convective

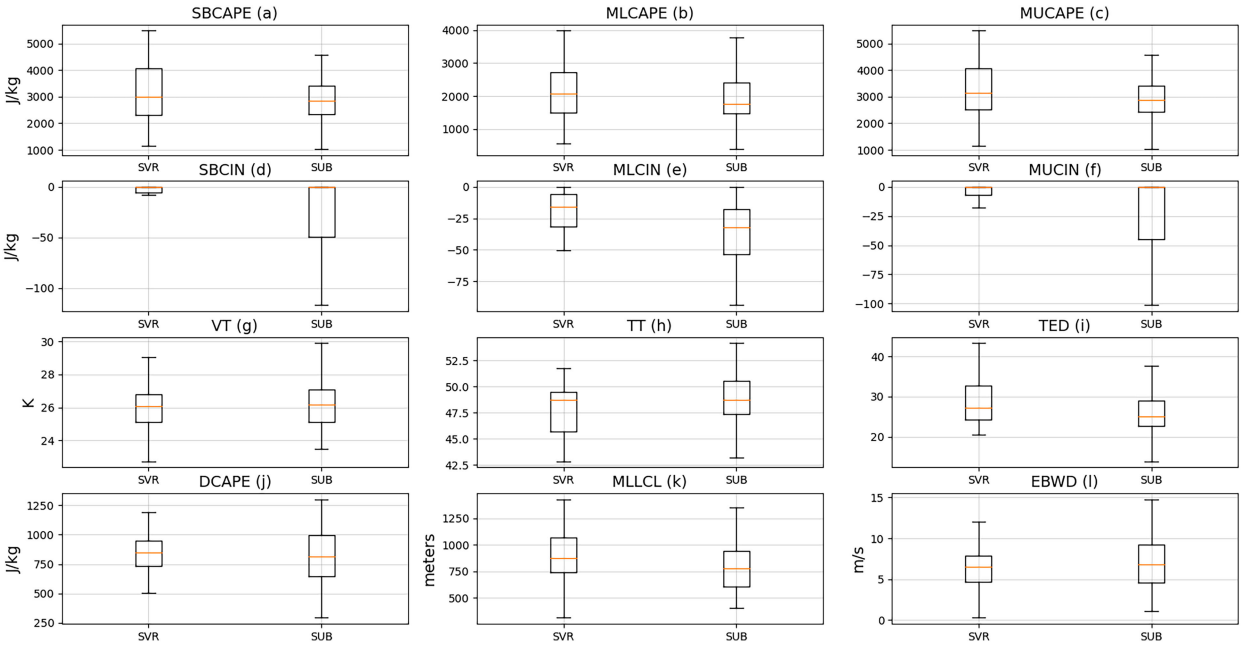

FIG. 11. As in Fig. 2, but classes are divided into CM1 initialization profiles that resulted in a simulation with SVR or subsevere (SUB) winds.

inhibition alone may not be sufficient for successful discrimination between severe and subsevere environments.

4. Probability of sampling severe wind: Simulated network experiments

a. *Creating simulated networks*

The wind swaths found in the eight downburst simulations with the largest spatial extent (10^1 km^2 or greater) of severe winds imply that a surface observing network with a maximum station separation $O(3)$ km would be required to sample winds over 26 m s^{-1}. While most research micronets have an average station spacing of around 2–5 km (AW91; Fiebrich and Crawford 2001; Basara et al. 2011; Gramsch et al. 2020), typical operational mesonets have average station spacings $O(30)$ km (see Table 1). By these metrics, the probability of observing a severe downburst wind gust by most modern observation networks is low. To quantify this probability more formally, three simple experiments are conducted in which a series of simulated observing networks are constructed over the 80 km × 80 km model domain. Each experiment is designed to replicate a typical mesonet (MESO), a typical research micronet (MICRO), and a replication of the observing network deployed during the MIST field campaign (AW91). In each experiment, 100 simulated networks are constructed with arbitrary station placement, but similar network density, over each of the 34 maximum wind swath grids that recorded severe winds. The number of simulated networks that "observe" severe winds is recorded and yields a rough estimate of the probability that a MESO, MICRO, or MIST observing network with random station placement would sample winds exceeding 26 m s^{-1}. Additional details of each experiment are given in Table 3.

The procedure for generating each simulated network and their respective "observations" is as follows. For each experiment, the minimum station spacing S of the simulated network is selected to reflect the desired network type. Koch et al. (1983) give a formula [Eq. (1)] for determining the average spacing between stations placed in a regular grid n_r over a domain with area A. Although the simulated networks in this study are not regularly spaced, this formula can be modified to yield an initial guess at the number of stations N needed for each network based on the desired network density. The primary modification is to assume Eq. (1) converges to Eq. (2) as N becomes large. It is then trivial to solve for the number of stations [Eq. (3)]:

$$\Delta n_r = A^{1/2}\left[\frac{(1 + N^{1/2})}{(N - 1)}\right], \tag{1}$$

$$\Delta n_r \approx \frac{A^{1/2}}{N^{1/2}}, \tag{2}$$

$$N \approx \frac{A}{\Delta n_r^2}. \tag{3}$$

A random X, Y point on the 80 km × 80 km model domain is chosen as a candidate location for an "observing station." The

TABLE 3. Simulated network experiment configurations.

Experiment name	Average station spacing	Number of stations	Number of networks
MESO	33.4 km	6	100
MICRO	5.2 km	170	100
MIST	2.3 km	800	100

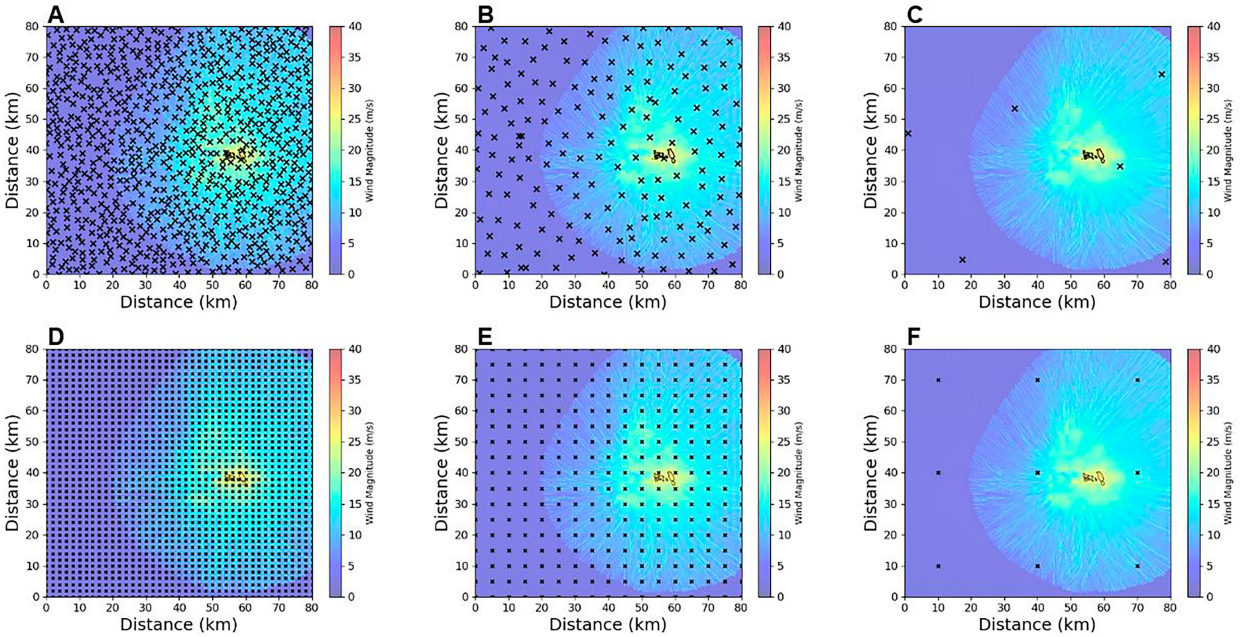

FIG. 12. An example of a simulated network with (top) random station placement and (bottom) gridded station placement for the (a),(d) MIST, (b),(e) MICRO, and (c),(f) MESO networks. Stations are denoted by the black "X" marks; the black contour denotes swaths of wind exceeding 26 m s^{-1}.

distances between this candidate point and all other stations already in the network are determined, and if the minimum separation distance is greater than S, then the candidate station is added to the network. If this check fails, then another random point is selected, and the process repeats until there are N stations in the network. (Note that the distance check is not required for the first station added to the network.)

After there are N stations in the network, the average minimum distance between stations is checked. If this average minimum distance does not match the desired network density, N is iteratively tuned to achieve the desired network density. Once S and N are determined, they are held constant to create 100 simulated networks with identical number of stations and network densities, but unique station placements. The maximum wind swath grid value at the nearest grid point was used as the "observed" wind. This process was repeated for each of the 34 simulations that produced winds in excess of 26 m s^{-1}, giving 3400 unique observing networks for each of the MESO, MICRO, and MIST experiments, a grand total of 10 200 observing networks across all three experiments. One such example from each network is presented in Fig. 12.

b. *Simulated network results*

After the observed winds are generated for the 3400 simulated networks, the probability that a MESO, MICRO, or MIST network would sample severe winds (or winds of any other threshold) can be determined. If a network contained at least one station that reached the threshold, then the network is considered a "hit." If no stations within the network reached the threshold, then it is considered a "miss." The number of networks that hit a certain wind threshold can be expressed as a percentage of the total number of networks for each maximum wind swath grid. This percentage is interpreted as the probability that an observing network with an average station spacing of S, but random station placement, will sample a given wind speed for a given downburst event.

The probabilities of sampling 15, 20, 22, and 26 m s^{-1} winds at different spatial scales for each experiment are given in Fig. 13. The average probability of sampling severe winds across any spatial scale is 43% in the MIST experiment, decreasing to 18% for the MICRO experiment and 0.7% for the MESO experiment. Figures 8 and 9 both support the idea that subsevere winds are more common in downbursts than severe winds, and Fig. 13 suggests that they have a higher probability of being sampled as a result. For example, nearly all networks in the MIST and MICRO experiments and 34% of the MESO networks sampled winds of at least 15 m s^{-1}. One caveat worth reiterating is that these experiments use 50-m wind speeds as a proxy for 10-m gusts. While observational studies support the idea that winds above the surface can mix down to typical surface-station observing heights in thunderstorm outflows (Gunter and Schroeder 2015; Canepa et al. 2020), it is not well documented how frequently this occurs and over what spatial scales for localized downbursts as opposed to other convective modes.

Nonetheless, two distinct relationships emerge from these results. The first is that for a given spatial coverage of winds at or above a set threshold, the probability of sampling the target threshold decreases with increasing station spacing. Comparing the percentage of networks with a successful sample across a given spatial threshold in Fig. 13 illustrates this idea. For example, the probability of sampling 26 m s^{-1} winds

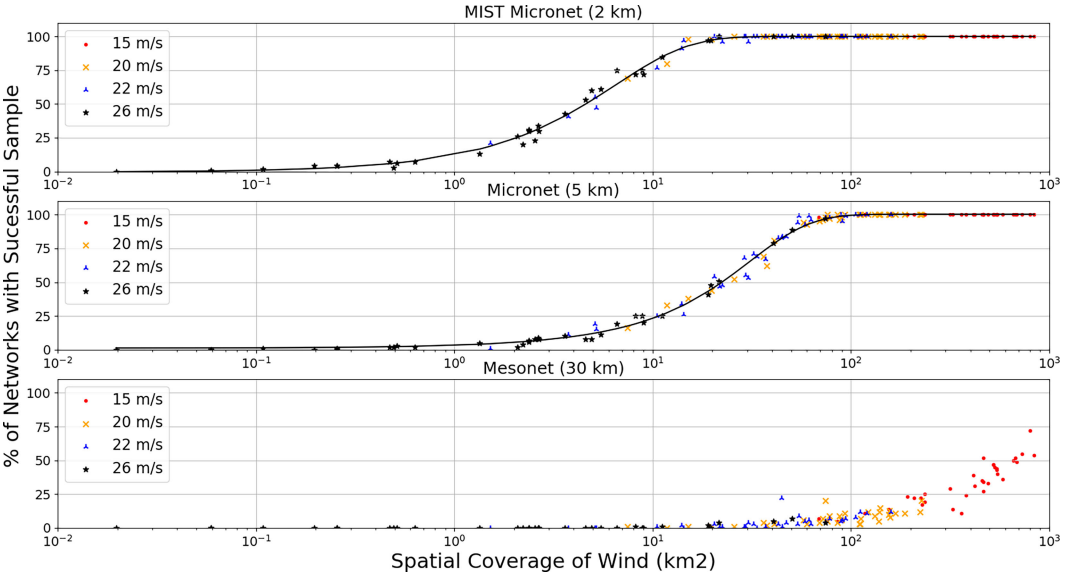

FIG. 13. Percentage of simulated networks that successfully sampled given wind thresholds (markers) using the (top) MIST, (middle) MICRO, and (bottom) MESO network configurations and the fitted logistic functions for the MIST and MICRO experiments (solid black line).

over an area of 10^1 km^2 decreases from approximately 80% in the MIST experiment to around 20% and <5% for the MICRO and MESO experiments, respectively. Similarly, sampling winds at or above any given threshold with an areal coverage of 10^2 km^2 is nearly guaranteed with the MIST and MICRO networks, but falls precipitously to below 25% for the MESO network.

The second relationship is that for a given wind speed threshold, the probability of sampling increases as a function of the spatial coverage of wind at or above the threshold, regardless of network density. This relationship can be observed in each of the experiment plots in Fig. 13 and is best described by a logistic equation (note that the MESO experiment did not contain enough data points to accurately fit a sigmoid curve). The only variable is at what spatial scale the probability of sampling begins to increase, and this appears to be directly related to station spacing within the observing network. For instance, note that the spatial scale at which sampling probability is 50% increases from 10^0 km^2 in the MIST (2.3-km spacing) experiment to 10^1 km^2 in the MICRO experiment (5.2-km spacing) and 10^2 km^2 in the MESO experiment (33.4-km spacing).

This relationship also suggests that there exists a spatial threshold [hereafter referred to as the minimum required area (MRA)] of a thunderstorm outflow at which sampling a target wind threshold is nearly guaranteed for each network. From signal processing, the Nyquist frequency dictates that the sampling frequency required in order to fully resolve a signal is $\frac{1}{2}$ the frequency of the target signal (Landau 1967). This concept is applicable to fully resolving atmospheric phenomenon as well. For example, consider a cross section of a circular downburst cold pool with a diameter of 6 km. The enhanced winds within the cold pool could theoretically go unsampled if they occurred within an observing network with a station spacing of 6 km or greater. However, if the station spacing is reduced by at least 0.5–3 km, then the cold pool is guaranteed to be sampled by at least one station. This example reflects a real-world scenario described briefly by Fujita (1981b). In other words, multiplying the station spacing S by two gives the smallest cold pool diameter that can be reliably resolved by the observing network in a single dimension. To account for the two-dimensional nature of downburst outflows at the surface, the product of $2S$ can be squared to give the minimum required area outflow winds at a certain threshold must achieve to be sampled [Eq. (4)]:

$$\text{minimum required area} = (2S)^2. \tag{4}$$

Consequently, this gives MRA values of 21.2, 108.2, and 4462.2 km^2 for the MIST, MICRO, and MESO networks, respectively, based on the average station spacings given in Table 3. These theoretical values are supported by the network simulation results in Fig. 13, although it is noted that the threshold value for the MESO experiment is off the abscissa of the figure as no simulation resulted in a coverage of 15 m s^{-1} $\geq$ 4462.2 km^2. For the MIST and MICRO networks, these MRA values can be input into their respective fitted logistic functions to yield probability values of 98% and 100%, respectively, which appears to validate the concept of an MRA. This relationship can be beneficial in network planning if the typical spatial scale of a target meteorological phenomenon (such as a convective downburst) is known. In more practical terms for severe weather verification, this result implies that a swath of severe downburst winds must be nearly 4500 km^2 to guarantee being sampled by most mesonets.

The probability of sampling severe winds by all networks might be improved slightly by utilizing a perfectly regular

gridded network. For each of the MIST, MICRO, and MESO experiments, a gridded network with a set station spacing of 2, 5, and 30 km, respectively, was created for each downburst wind field (e.g., Figs. 12d,e). Essentially, this yields the same simulated observation network sampling 34 different wind fields, which can then be used to answer the question: "Given a regular gridded network with station spacing S, what is the probability of sampling a certain wind threshold for any random severe downburst wind field?" The regularly gridded MIST network sampled winds at or above 22 m s^{-1} in every downburst wind field and captured 50% of the severe wind swaths. The other networks had worse performance, sampling severe winds in only 21% (MICRO) and 6% (MESO) of the downbursts. However, these statistics represent the potential for improved performance over networks with arbitrary station placement.

5. Summary and discussion

In this study, the statistical distribution of near-surface wind speeds within single-cell wet downburst outflows is amalgamated from a collection of 97 high-resolution CM1 simulations. Such statistical descriptions may give forecasters and researchers a better understanding of the potential impacts from wet downbursts and their propensity for producing winds above certain thresholds. These simulations also present the opportunity to assess the capabilities of modern observing networks to adequately sample 26+ m s^{-1} winds associated with severe downbursts via a series of simulated observing network experiments. The results from the simulations and network experiments point to three main conclusions.

First, the CM1 simulations suggest that the frequency of damaging downbursts featuring severe winds is only 35%. Another way to interpret this result is that if a WFT produces a wind damage report, then there is a 35% chance that the downburst produced severe winds. Miller and Mote (2017b) noted that only 0.6% of all WFTs in their sample were associated with a severe report of any kind. If one knowingly makes the incorrect assumption that all reports were associated with damaging winds, then severe WFTs would account for only 0.2% of all WFTs, though the true number is likely lower. Such a small percentage of the total WFT population and the considerable environmental overlap between severe and subsevere downburst environments (Fig. 11) underscore the difficulty in correctly identifying severe WFTs. The small spatial and temporal footprints of severe wind swaths further complicate the SVR warning decision-making process.

Second, the simulated network results suggest that an average station spacing of 1.58 km or less would be required to reliably sample swaths of severe winds in WFT downbursts. Few operational observing networks meet this criterion, and the low (0.7%) probability for a typical mesoscale network to measure a wind gust over 26 m s^{-1} in a severe downburst introduces the potential for mischaracterizing a severe thunderstorm as subsevere. However, a combination of different observing networks deployed over the same geographic region may meet these 1.58-km criteria and help alleviate the potential for undersampling. A real-world example is given by Childs et al. (2021), who documented the destructive macroburst over Akron, Colorado, on 9 June 2020. Although the thermodynamic and kinematic environments in the 9 June event were considerably different than those studied here, a single convective cell produced a swath of nearly 51 m s^{-1} (100 kt) winds that were undersampled by regional ASOS stations, which were approximately 40 km apart. Instead, peak wind speeds were observed by a denser clustering of agricultural and home weather stations. In the absence of a sufficiently dense network, surface observations should be used with caution when making judgments on WFT events.

Finally, the higher frequency of occurrence and greater spatial footprints of subsevere winds found in this study suggest that wind damage—especially tree damage—is more likely attributable to subsevere winds rather than severe winds, owing to the higher probability for subsevere winds to impact a potential damage indicator. Frelich and Ostuno (2012) and Schindler et al. (2012) explored how a myriad of factors (species, age, health, diameter, soil type and moisture, root anchoring, etc.) can result in tree damage at subsevere wind speeds, and numerical studies by Gardiner et al. (2000), Schelhaas et al. (2007), and Dupont et al. (2015) indicate that tree damage can begin with canopy-level wind speeds between 10 and 20 m s^{-1}. This has implications for SVR warning decision-making since impacts can occur at wind speeds that are below the current NWS severe wind threshold but constitute a large portion of a typical downburst wind field. This also challenges the use of tree damage reports as verifying records for SVR warnings based on the current wording of NWS Directive 10-511, which states that a SVR warning should be issued "when there is radar or satellite indication and/or reliable reports of wind gusts equal to or in excess of 50 kt [58 miles per hour (mph)] and/or hail size of 1 in. (U.S. quarter size) in diameter or larger." Flexible warning criteria and/or different warning or messaging strategies may be needed to better serve the public depending on the propensity for native vegetation to experience impacts at subsevere wind speeds. Explicit details regarding regional impacts and warning criteria are beyond the scope of this study but should be investigated to augment NWS warning service to the public.

Comparisons to observed downbursts lend reasonable confidence to the validity of these three conclusions. However, several factors could influence the exact quantifications presented herein. While the impact to peak wind speed was small (2.4%), increasing the grid spacing did yield a stronger downburst with a larger outflow radius. This suggests that peak wind velocities may be underresolved in these simulations. The influence of terrain was not considered but could have a substantial impact on near-surface wind speeds (Abd-Elaal et al. 2018). Furthermore, sensitivity to the semislip lower boundary condition and friction parameterization utilized in the simulations were not explicitly tested but may influence low-level velocities (Vermeire et al. 2011). Each of these factors represents an opportunity for future research, but no single factor is expected to be influential enough to significantly alter the overarching findings of this study.

The fact that severe winds were simulated within WFT downbursts is not inherently new nor unexpected based on past observational and simulated studies, but the quantification of the frequency, duration, and spatial coverage of severe wind swaths bolsters our understanding of WFT downburst events. In turn, this exposes the weakness of modern observation networks in their ability to sample the peak winds of a downburst. Future observational studies endeavoring to sample downburst winds in the same spirit as the early field campaigns should now have a better understanding of the station spacing requirements. This also demonstrates the need for, and potential benefit of, denser observational networks, including the use of regional agricultural networks or private weather stations as in Childs et al. (2021). The results from this study also highlight the warning challenges associated with WFT downburst events. Even when correctly identified, the average SVR warning may contain considerable false alarm in both time and space. This is compounded by the likelihood that tree damage is occurring at wind speeds below current NWS SVR warning criteria. By extension, this calls into question the current practice of using tree damage reports as verifying events for warnings and the appropriateness of using a 26 m s^{-1} wind threshold to capture true societal impacts. Finally, this study presents future opportunities to test previously proposed parameters and methodologies for severe WFT downburst forecasting, as well as develop new metrics and tools that will ultimately aid in the forecast process.

Acknowledgments. The author would like to extend thanks to his colleagues at the Storm Prediction Center for their support, feedback, and interest in this project. Specifically, thanks are given to Andy Dean and Ryan Jewell for LSR and sounding data acquisition and Israel Jirak for thorough feedback and advice throughout the project. Additional thanks are given to the reviewers who offered thoughtful insights and advice that fortified this study. The computing for this project was performed at the OU Supercomputing Center for Education & Research (OSCER) at the University of Oklahoma (OU).

Data availability statement. The CM1 namelist used in this study, as well as the entirety of the candidate sounding dataset, including the subset of soundings used to initialize the CM1 simulations, are available upon request of the author. The CM1 code can be downloaded at https://www2.mmm.ucar.edu/people/bryan/cm1/. Wind damage LSRs are provided by the National Centers for Environmental Information and can be downloaded at https://www.ncdc.noaa.gov/stormevents/ftp.jsp.

REFERENCES

Abd-Elaal, E.-S., J. E. Mills, and X. Ma, 2018: Numerical simulation of downburst wind, flow over real topography. *J. Wind Eng. Ind. Aerodyn.*, **172**, 85–95, https://doi.org/10.1016/j.jweia.2017.10.026.

Adgas, D., G. D. Webster, and F. J. Masters, 2012: Wind speed perception and risk. *PLOS ONE*, **7**, e49944, https://doi.org/10.1371%2Fjournal.pone.0049944.

Anabor, V., U. Rizza, E. L. Nascimento, and G. A. Degrazia, 2011: Large-eddy simulation of a microburst. *Atmos. Chem. Phys.*, **11**, 9323–9331, https://doi.org/10.5194/acp-11-9323-2011.

Anderson-Frey, A. K., Y. P. Richardson, A. R. Dean, R. L. Thompson, and B. T. Smith, 2016: Investigation of near-storm environments for tornado events and warnings. *Wea. Forecasting*, **31**, 1771–1790, https://doi.org/10.1175/WAF-D-16-0046.1.

Armfield, S. W., 1991: Finite difference solutions of the Navier-Stokes equations on staggered and non-staggered grids. *Comput. Fluids*, **20**, 1–17, https://doi.org/10.1016/0045-7930(91)90023-B.

Atkins, N. T., and R. M. Wakimoto, 1991: Wet microburst activity over the southeastern United States: Implications for forecasting. *Wea. Forecasting*, **6**, 470–482, https://doi.org/10.1175/1520-0434(1991)006<0470:WMAOTS>2.0.CO;2.

Atlas, D., C. W. Ulbrich, and C. R. Williams, 2004: Physical origin of a wet microburst: Observations and theory. *J. Atmos. Sci.*, **61**, 1186–1195, https://doi.org/10.1175/1520-0469(2004)061<1186:POOAWM>2.0.CO;2.

Basara, J. B., and Coauthors, 2011: The Oklahoma City micronet. *Meteor. Appl.*, **18**, 252–261, https://doi.org/10.1002/met.189.

Benjamin, S. G., and Coauthors, 2004: An hourly assimilation-forecast cycle: The RUC. *Mon. Wea. Rev.*, **132**, 495–518, https://doi.org/10.1175/1520-0493(2004)132<0495:AHACTR>2.0.CO;2.

Bolgiani, P., D. Santos-Muñoz, S. Fernández-González, M. Sastre, F. Valero, and M. L. Martín, 2020: Microburst detection with the WRF model: Effective resolution and forecasting indices. *J. Geophys. Res. Atmos.*, **125**, e2020JD032883, https://doi.org/10.1029/2020JD032883.

Bothwell, P. D., J. Hart, and R. L. Thompson, 2002: An integrated three-dimensional objective analysis scheme in use at the storm prediction center. Preprints, *21st Conf. on Severe and Local Storms*, San Antonio, TX, Amer. Meteor. Soc., JP3.1, https://www.spc.noaa.gov/publications/bothwell/sfcoa.pdf.

Brock, F. V., K. C. Crawford, R. L. Elliott, G. W. Cuperus, S. J. Stadler, H. L. Johnson, and M. D. Eilts, 1995: The Oklahoma mesonet: A technical overview. *J. Atmos. Oceanic Technol.*, **12**, 5–19, https://doi.org/10.1175/1520-0426(1995)012<0005:TOMATO>2.0.CO;2.

Brooks, H. E., 1992: Operational implications of the sensitivity of modelled thunderstorms to thermal perturbations. Preprints, *Fourth AES/CMOS Workshop on Operational Meteorology*, Whistler, British Columbia, Canada, Atmospheric and Environmental Service and Canadian Meteorological and Oceanographic Society, 398–407, https://www.flame.org/~cdoswell/publications/Brooks_AES_CMOS.pdf.

Brotzge, J. A., S. E. Nelson, R. L. Thompson, and B. T. Smith, 2013: Tornado probability of detection of lead time as a function of convective mode and environmental parameters. *Wea. Forecasting*, **28**, 1261–1276, https://doi.org/10.1175/WAF-D-12-00119.1.

——, and Coauthors, 2020: A technical overview of the New York State Mesonet standard network. *J. Atmos. Oceanic Technol.*, **37**, 1827–1845, https://doi.org/10.1175/JTECH-D-19-0220.1.

Brown, M. C., C. J. Nowotarski, A. R. Dean, B. T. Smith, R. L. Thompson, and J. M. Peters, 2021: The early evening transition in southeastern U.S. tornado environments. *Wea. Forecasting*, **36**, 1431–1452, https://doi.org/10.1175/WAF-D-20-0191.1.

Bryan, G. H., and J. M. Fritsch, 2002: A benchmark simulation for moist nonhydrostatic numerical models. *Mon. Wea. Rev.*, **130**, 2917–2928, https://doi.org/10.1175/1520-0493(2002)130<2917:ABSFMN>2.0.CO;2.

——, J. C. Wyngaard, and J. M. Fritsch, 2003: Resolution requirements for the simulation of deep moist convection. *Mon. Wea. Rev.*, **131**, 2394–2416, https://doi.org/10.1175/1520-0493(2003)131<2394:RRFTSO>2.0.CO;2.

Byers, H. R., and R. R. Braham Jr., 1948: Thunderstorm structure and circulation. *J. Atmos. Sci.*, **5**, 71–86, https://doi.org/10.1175/1520-0469(1948)005%3C0071:TSAC%3E2.0.CO;2.

Canepa, F., M. Burlando, and G. Solari, 2020: Veritical profile characteristics of thunderstorm outflows. *J. Wind Eng. Ind. Aerodyn.*, **206**, 104332, https://doi.org/10.1016/j.jweia.2020.104332.

Caracena, F., and M. W. Maier, 1987: Analysis of a microburst in the FACE meteorological mesonetwork in southern Florida. *Mon. Wea. Rev.*, **115**, 969–985, https://doi.org/10.1175/1520-0493(1987)115<0969:AOAMIT>2.0.CO;2.

Chandrakar, K. K., W. W. Grabowski, H. Morrison, and G. H. Bryan, 2021: Impact of entrainment mixing and turbulent fluctuation on droplet size distributions in a cumulus cloud: An investigation using Lagrangian microphysics with a subgrid-scale model. *J. Atmos. Sci.*, **78**, 2983–3005, https://doi.org/10.1175/JAS-D-20-0281.1.

Chay, M. T., F. Albermani, and R. Wilson, 2006: Numerical and analytical simulation of downburst winds. *Eng. Struct.*, **28**, 240–254, https://doi.org/10.1016/j.engstruct.2005.07.007.

Childs, S. J., R. S. Schumacher, and R. D. Adams-Selin, 2021: High resolution observations of a destructive macroburst. *Mon. Wea. Rev.*, **149**, 2875–2896, https://doi.org/10.1175/MWR-D-20-0412.1.

Choi, E. C. C., and F. A. Hidayat, 2002: Gust factors for thunderstorm and non-thunderstorm winds. *J. Wind Eng. Ind. Aerodyn.*, **90**, 1683–1696, https://doi.org/10.1016/S0167-6105(02)00279-9.

Coffer, B. E., and M. D. Parker, 2015: Impacts of increasing low-level shear on supercells during the early evening transition. *Mon. Wea. Rev.*, **143**, 1945–1969, https://doi.org/10.1175/MWR-D-14-00328.1.

——, ——, J. M. Dahl, L. J. Wicker, and A. J. Clark, 2017: Volatility of tornadogenesis: An ensemble of simulated nontornadic and tornadic supercells in VORTEX2 environments. *Mon. Wea. Rev.*, **145**, 4605–4625, https://doi.org/10.1175/MWR-D-17-0152.1.

Coniglio, M. C., 2012: Verification of RUC 0-1-h forecasts and SPC mesoscale analyses using VORTEX2 soundings. *Wea. Forecasting*, **27**, 667–683, https://doi.org/10.1175/WAF-D-11-00096.1.

——, and R. E. Jewell, 2022: SPC mesoscale analysis compared to field-project soundings: Implications for supercell environment studies. *Mon. Wea. Rev.*, **150**, 567–588, https://doi.org/10.1175/MWR-D-21-0222.1.

Cook, N. J., 2022: Locating the anemometers of the US ASOS network and classifying their local shelter. *Weather*, **77**, 256–263, https://doi.org/10.1002/wea.4131.

Dabberdt, W. F., and Coauthors, 2005: Multifunctional mesoscale observing networks. *Bull. Amer. Meteor. Soc.*, **86**, 961–982, https://doi.org/10.1175/BAMS-86-7-961.

Dahl, N. A., I. L. Jirak, K. H. Knopfmeier, J. Martin, and B. C. Matilla, 2022: Warn-on-forecast system output as a verification tool for severe wind events. *Proc. 30th Conf. Severe Local Storms*, Santa Fe, NM, Amer. Meteor. Soc., 17.3B, https://www.spc.noaa.gov/publications/dahl/wofsverf.pdf.

Deardorff, J., 1980: Stratocumulus-capping mixed layers derived from a three-dimensional model. *Bound.-Layer Meteor.*, **18**, 495–527, https://doi.org/10.1007/BF00119502.

Dodge, J., J. Arnolds, G. Wilson, J. Evans, and T. Fujita, 1986: The Cooperative Huntsville Meteorological Experiment (COHMEX). *Bull. Amer. Meteor. Soc.*, **67**, 417–419.

Doswell, C. A., III, H. E. Brooks, and M. P. Kay, 2005: Climatological estimates of daily local nontornadic severe thunderstorm probability for the United States. *Wea. Forecasting*, **20**, 577–595, https://doi.org/10.1175/WAF866.1.

Dupont, S., D. Pivato, and Y. Brunet, 2015: Wind damage propagation in forests. *Agric. For. Meteor.*, **214–215**, 243–251, https://doi.org/10.1016/j.agrformet.2015.07.010.

Edwards, R., J. T. Allen, and G. W. Carbin, 2018: Reliability and climatological impacts of convective wind estimations. *J. App. Meteor. Climatol.*, **57**, 1825–1845, https://doi.org/10.1175/JAMC-D-17-0306.1.

Emrich, C. T., and S. L. Cutter, 2011: Social vulnerability to climate-sensitive hazards in the southern United States. *Wea. Climate Soc.*, **3**, 193–208, https://doi.org/10.1175/2011WCAS1092.1.

Fiebrich, C. A., and K. C. Crawford, 2001: The impact of unique meteorological phenomena detected by the Oklahoma mesonet and ARS micronet on automated quality control. *Bull. Amer. Meteor. Soc.*, **82**, 2173–2188, https://doi.org/10.1175/1520-0477(2001)082<2173:TIOUMP>2.3.CO;2.

Foster, D. S., 1958: Thunderstorm gusts compared with computed downdraft speeds. *Mon. Wea. Rev.*, **86**, 91–94, https://doi.org/10.1175/1520-0493(1958)086<0091:TGCWCD>2.0.CO;2.

Frelich, L. E., and E. J. Ostuno, 2012: Estimating wind speeds of convective storms from tree damage. *Electron. J. Severe Storms Meteor.*, **7** (9), https://doi.org/10.55599/ejssm.v7i9.45.

Fujita, T. T., 1978: Manual of downburst identification for project NIMROD. SMRP Res. Paper 156, 104 pp., NTIS PB-286048, https://ntrs.nasa.gov/api/citations/19780022828/downloads/19780022828.pdf?attachment=true.

——, 1981a: Microbursts as an aviation wind shear hazard. *19th Aerospace Sciences Meeting*, St. Louis, MO, American Institute of Aeronautics and Astronautics, AIAA-81-0386, https://doi.org/10.2514/6.1981-386.

——, 1981b: Tornadoes and downbursts in the context of generalized planetary scale. *J. Atmos. Sci.*, **38**, 1511–1534, https://doi.org/10.1175/1520-0469(1981)038<1511:TADITC>2.0.CO;2.

——, 1985: *The Downburst: Microburst and Macrobrust: Report of Projects NIMROD and JAWS*. Satellite and Mesometeorology Research Project (SMRP), Department of Geophysical Sciences, University of Chicago, 122 pp.

——, 1990: Downbursts: Meteorological features and wind field characteristics. *J. Wind Eng. Ind. Aerodyn.*, **36**, 75–86, https://doi.org/10.1016/0167-6105(90)90294-M.

——, and R. M. Wakimoto, 1981: Five scales of airflow associated with a series of downbursts on 16 July 1980. *Mon. Wea. Rev.*, **109**, 1438–1456, https://doi.org/10.1175/1520-0493(1981)109<1438:FSOAAW>2.0.CO;2.

Gardiner, B., H. Peltola, and S. Kellomaki, 2000: Comparison of two models for predicting the critical wind speeds required to damage coniferous trees. *Ecol. Modell.*, **129** (1), 1–23, https://doi.org/10.1016/S0304-3800(00)00220-9.

Grams, J. S., R. L. Thompson, D. V. Snively, J. A. Prentice, G. M. Hodges, and L. J. Reames, 2012: A climatology and comparison of parameters for significant tornado events in

the United States. *Wea. Forecasting*, **27**, 106–123, https://doi.org/10.1175/WAF-D-11-00008.1.

Gramsch, E., L. Morales, M. Baeza, C. Ayala, C. Soto, J. Neira, P. Perez, and F. Moreno, 2020: Citizens' surveillance micronetwork for the mapping of PM2.5 in the city of Concon, Chile. *Aerosol Air Qual. Res.*, **20**, 358–368, https://doi.org/10.4209/aaqr.2019.04.0179.

Guillot, E. M., T. M. Smith, V. Lakshmanan, K. L. Elmore, D. W. Burgess, and G. J. Stumpf, 2008: Tornado and severe thunderstorm warning forecast skill and its relationship to storm type. Preprints, *24th Int. Conf. on Interactive Information Processing Systems for Meteorology, Oceanography, and Hydrology*, New Orleans, LA, Amer. Meteor. Soc., 4A.3. https://ams.confex.com/ams/pdfpapers/132244.pdf.

Gunter, W. S., and J. L. Schroeder, 2015: High-resolution, full-scale measurements of thunderstorm outflow winds. *J. Wind Eng. Ind. Aerodyn.*, **138**, 13–26, https://doi.org/10.1016/j.jweia.2014.12.005.

Harrison, D. R., and C. D. Karstens, 2017: A climatology of operational storm-based warnings: A geospatial analysis. *Wea. Forecasting*, **32**, 47–60, https://doi.org/10.1175/WAF-D-15-0146.1.

Hart, J. A., and W. Korotky, 1991: The SHARP workstation v1.50 users guide. NOAA/National Weather Service, 30 pp.

Herman, G. R., E. R. Nielsen, and R. S. Schumacher, 2018: Probabilistic verification of storm prediction center convective outlooks. *Wea. Forecasting*, **33**, 161–184, https://doi.org/10.1175/WAF-D-17-0104.1.

Hiris, Z. A., and W. A. Gallus Jr., 2021: On the relationship of cold pool and bulk shear magnitudes on upscale convective growth in the Great Plains of the United States. *Atmosphere*, **12**, 1019, https://doi.org/10.3390/atmos12081019.

Hjelmfelt, M. R., 1988: Structure and life cycle of microburst outflow observed in Colorado. *J. Appl. Meteor.*, **27**, 900–927, https://doi.org/10.1175/1520-0450(1988)027<0900:SALCOM>2.0.CO;2.

Horel, J., and Coauthors, 2002: Mesowest: Cooperative mesonets in the western United States. *Bull. Amer. Meteor. Soc.*, **83**, 211–226, https://doi.org/10.1175/1520-0477(2002)083<0211:MCMITW>2.3.CO;2.

Jirak, I. L., C. J. Melick, and S. J. Weiss, 2014: Combining probabilistic ensemble information from the environment with simulated storm attributes to generate calibrated probabilities of severe weather hazards. *27th Conf. on Severe Local Storms*, Madison, WI, Amer. Meteor. Soc., 2.5, https://www.spc.noaa.gov/publications/jirak/calprob.pdf.

Kim, J., and H. Hangan, 2007: Numerical simulations of impinging jets with application to downbursts. *J. Wind Eng. Ind. Aerodyn.*, **95**, 279–298, https://doi.org/10.1016/j.jweia.2006.07.002.

Kingsmill, D. E., and R. M. Wakimoto, 1991: Kinematic, dynamic, and thermodynamic analysis of a weakly sheared severe thunderstorm over northern Alabama. *Mon. Wea. Rev.*, **119**, 262–297, https://doi.org/10.1175/1520-0493(1991)119<0262:KDATAO>2.0.CO;2.

Koch, S. E., M. DesJardins, and P. J. Kocin, 1983: An interactive Barnes objective map analysis scheme for use with satellite and conventional data. *J. Climate Appl. Meteor.*, **22**, 1487–1503, https://doi.org/10.1175/1520-0450(1983)022<1487:AIBOMA>2.0.CO;2.

Lagerquist, R., A. McGovern, and T. Smith, 2017: Machine learning for real-time prediction of damaging straight-line convective wind. *Wea. Forecasting*, **32**, 2175–2193, https://doi.org/10.1175/WAF-D-17-0038.1.

Landau, H. J., 1967: Sampling, data transmission, and the Nyquist rate. *Proc. IEEE*, **55**, 1701–1706, https://doi.org/10.1109/PROC.1967.5962.

Lane, T. P., and R. D. Sharman, 2014: Intensity of thunderstorm-generated turbulence revealed by large-eddy simulation. *Geophys. Res. Lett.*, **41**, 2221–2227, https://doi.org/10.1002/2014GL059299.

Lee, W.-C., R. E. Carbone, and R. M. Wakimoto, 1992: The evolution and structure of a "bow-echo–microburst" event. Part I: The microburst. *Mon. Wea. Rev.*, **120**, 2188–2210, https://doi.org/10.1175/1520-0493(1992)120<2188:TEASOA>2.0.CO;2.

Lombardo, F. T., and A. S. Zickar, 2019: Characteristics of measured extreme thunderstorm near-surface wind gusts in the United States. *J. Wind Eng. Ind. Aerodyn.*, **193**, 103961, https://doi.org/10.1016/j.jweia.2019.103961.

Markowski, P., and Y. Richardson, 2010: *Mesoscale Meteorology in Midlatitudes*. 1st ed. Wiley-Blackwell, 432 pp.

Markowski, P. M., 2016: An idealized numerical simulation investigation of the effects of surface Drag on the development of near-surface vertical vorticity in supercell thunderstorms. *J. Atmos. Sci.*, **73**, 4349–4385, https://doi.org/10.1175/JAS-D-16-0150.1.

——, and G. H. Bryan, 2016: LES of laminar flow in the PBL: A potential problem for convective storm simulations. *Mon. Wea. Rev.*, **144**, 1841–1850, https://doi.org/10.1175/MWR-D-15-0439.1.

Mason, M. S., G. S. Wood, and D. F. Fletcher, 2009: Numerical simulations of downburst winds. *J. Wind Eng. Ind. Aerodyn.*, **97**, 523–539, https://doi.org/10.1016/j.jweia.2009.07.010.

——, D. F. Fletcher, and G. S. Wood, 2010: Numerical simulation of idealized three-dimensional downburst wind fields. *Eng. Struct.*, **32**, 3558–3570, https://doi.org/10.1016/j.engstruct.2010.07.024.

May, R. M., and Coauthors, 2022: MetPy: A meteorological Python library for data analysis and visualization. *Bull. Amer. Meteor. Soc.*, **103**, E2273–E2284, https://doi.org/10.1175/BAMS-D-21-0125.1.

McCann, D. W., 1994: WINDEX—A new index for forecasting microburst potential. *Wea. Forecasting*, **9**, 532–541, https://doi.org/10.1175/1520-0434(1994)009<0532:WNIFFM>2.0.CO;2.

McCarthy, J., J. W. Wilson, and T. T. Fujita, 1982: The joint airport weather studies project. *Bull. Amer. Meteor. Soc.*, **63**, 15–22, https://doi.org/10.1175/1520-0477(1982)063<0015:TJAWSP>2.0.CO;2.

McPherson, R. A., and Coauthors, 2007: Statewide monitoring of the mesoscale environment: A technical update on the Oklahoma mesonet. *J. Atmos. Oceanic Technol.*, **24**, 301–321, https://doi.org/10.1175/JTECH1976.1.

Miller, P. W., and T. L. Mote, 2017a: Standardizing the definition of a "Pulse" thunderstorm. *Bull. Amer. Meteor. Soc.*, **98**, 905–913, https://doi.org/10.1175/BAMS-D-16-0064.1.

——, and Mote, T., 2017b: A climatology of weakly forced and pulse thunderstorms in the southeast United States. *J. Appl. Meteor. Climatol.*, **56**, 3017–3033, https://doi.org/10.1175/JAMC-D-17-0005.1.

——, and T. L. Mote, 2018: Characterizing severe weather potential in synoptically weakly forced thunderstorm environments. *Nat. Hazards Earth Syst. Sci.*, **18**, 1261–1277, https://doi.org/10.5194/nhess-18-1261-2018.

——, A. W. Black, C. A. Williams, and J. A. Knox, 2016a: Quantitative assessment of human wind speed overestimation. *J.*

Appl. Meteor. Climatol., **55**, 1009–1020, https://doi.org/10.1175/JAMC-D-15-0259.1.

——, ——, ——, and ——, 2016b: Maximum wind gusts associated with human-reported non-convective wind events and a comparison to current warning issuance criteria. *Wea. Forecasting*, **31**, 451–465, https://doi.org/10.1175/waf-d-15-0112.1.

Mohr, S., M. Kunz, A. Richter, and B. Ruck, 2017: Statistical characteristics of convective wind gusts in Germany. *Nat. Hazards Earth Syst. Sci.*, **17**, 957–969, https://doi.org/10.5194/nhess-17-957-2017.

Morrison, H., J. A. Curry, and V. I. Khvorostyanov, 2005: A new double-moment microphysics parameterization for application in cloud and climate models. Part 1: Description. *J. Atmos. Sci.*, **62**, 1665–1677, https://doi.org/10.1175/JAS3446.1.

NTSB, 1986: Aircraft accident report: Delta Airlines Inc., Lockheed L-1011-385-1. NTSB/AAR-86/05, 167 pp., www.ntsb.gov/investigations/AccidentReports/Reports/AAR8605.pdf.

Oreskovic, C., L. G. Orf, and E. Savory, 2018: A parametric study of downbursts using a full-scale cooling source model. *J. Wind Eng. Ind. Aerodyn.*, **180**, 168–181, https://doi.org/10.1016/j.jweia.2018.07.020.

Orf, L. G., and J. R. Anderson, 1999: A numerical study of traveling microbursts. *Mon. Wea. Rev.*, **127**, 1244–1258, https://doi.org/10.1175/1520-0493(1999)127<1244:ANSOTM>2.0.CO;2.

——, ——, and J. M. Straka, 1996: A three-dimensional numerical analysis of colliding microburst outflow dynamics. *J. Atmos. Sci.*, **53**, 2490–2511, https://doi.org/10.1175/1520-0469(1996)053<2490:ATDNAO>2.0.CO;2.

Orf, L., E. Kantor, and E. Savory, 2012: Simulation of a downburst-producing thunderstorm using a very high-resolution three-dimensional cloud model. *J. Wind Eng. Ind. Aerodyn.*, **104–106**, 547–557, https://doi.org/10.1016/j.jweia.2012.02.020.

——, R. Wilhelmson, B. Lee, C. Finley, and A. Houston, 2017: Evolution of a long-track violent tornado within a simulated supercell. *Bull. Amer. Meteor. Soc.*, **98**, 45–68, https://doi.org/10.1175/BAMS-D-15-00073.1.

Parker, M. D., 2017: How much does "backing aloft" actually impact a supercell? *Wea. Forecasting*, **32**, 1937–1957, https://doi.org/10.1175/WAF-D-17-0064.1.

Potvin, C. K., K. L. Elmore, and S. J. Weiss, 2010: Assessing the impacts of proximity sounding criteria on the climatology of significant tornado environments. *Wea. Forecasting*, **25**, 921–930, https://doi.org/10.1175/2010WAF2222368.1.

Proctor, F. H., 1988: Numerical simulations of an isolated microburst. Part I: Dynamics and structure. *J. Atmos. Sci.*, **45**, 3137–3160, https://doi.org/10.1175/1520-0469(1988)045<3137:NSOAIM>2.0.CO;2.

——, 1989: Numerical simulations of an isolated microburst. Part II: Sensitivity experiments. *J. Atmos. Sci.*, **46**, 2143–2165, https://doi.org/10.1175/1520-0469(1989)046<2143:NSOAIM>2.0.CO;2.

——, 1994: Case study of a low-reflectivity pulsating microburst: Numerical simulation of the Denver, 8 July 1989, storm. NTRS–NASA Tech. Rep. N95-10569, 4 pp., https://ntrs.nasa.gov/api/citations/19950004157/downloads/19950004157.pdf?attachment=true.

Pryor, K. L., 2015: Progress and developments of downburst prediction applications of GOES. *Wea. Forecasting*, **30**, 1182–1200, https://doi.org/10.1175/WAF-D-14-00106.1.

——, and G. P. Ellrod, 2005: GOES WMSI-progress and developments. Preprints, *21st Conf. on Weather Analysis and Forecasting*, Washington, DC, Amer. Meteor. Soc., P1.57, https://ams.confex.com/ams/pdfpapers/94155.pdf.

Rinehart, R., and M. Isaminger, 1986: Radar characteristics of microbursts in the mid-south. Preprints, *23rd Conf. on Radar Meteorology*, Snowmass, CO, Amer. Meteor. Soc. 116–119.

Romanic, D., and H. Hangan, 2020: Experimental investigation of the interaction between near-surface atmospheric boundary layer winds and downburst outflows. *J. Wind Eng. Ind. Aerodyn.*, **205**, 104323, https://doi.org/10.1016/j.jweia.2020.104323.

——, M. Taszarek, and H. Brooks, 2022: Convective environments leading to microburst, macroburst, and downburst events across the United States. *Wea. Climate Extremes*, **37**, 100474, https://doi.org/10.1016/j.wace.2022.100474.

Schelhaas, M. J., K. Kramer, H. Peltola, D. C. ver der Werf, and S. M. J. Wijdeven, 2007: Introducing tree interactions in wind damage simulation. *Ecol. Modell.*, **207**, 197–209, https://doi.org/10.1016/j.ecolmodel.2007.04.025.

Schindler, D., J. Bauhus, and H. Mayer, 2012: Wind effects on trees. *Eur. J. For. Res.*, **131**, 159–163, https://doi.org/10.1007/s10342-011-0582-5.

Schoen, J. M., and W. S. Ashley, 2011: A climatology of fatal convective wind events by storm type. *Wea. Forecasting.*, **26**, 109–121, https://doi.org/10.1175/2010WAF2222428.1.

Schroeder, J. L., W. S. Burgett, K. B. Haynie, I. Sonmez, G. D. Skwira, A. L. Doggett, and J. W. Lipe, 2005: The West Texas mesonet: A technical overview. *J. Atmos. Oceanic Technol.*, **22**, 211–222, https://doi.org/10.1175/JTECH-1690.1.

Schumacher, R. S., S. J. Childs, and R. D. Adams-Selin, 2023: Intense surface winds from gravity wave breaking in simulations of a destructive macroburst. *Mon. Wea. Rev.*, **151**, 775–793, https://doi.org/10.1175/MWR-D-22-0103.1.

Shu, Z. R., Q. S. Li, Y. C. He, and P. W. Chan, 2015: Gust factors for tropical cyclone, monsoon, and thunderstorm winds. *J. Wind Eng. Ind. Aerodyn.*, **142**, 1–14, https://doi.org/10.1016/j.jweia.2015.02.003.

Smith, B. T., T. E. Castellanos, A. C. Winters, C. M. Mead, A. R. Dean, and R. L. Thompson, 2013: Measured severe convective wind climatology and associated convective modes of thunderstorms in the contiguous United States, 2003–09. *Wea. Forecasting*, **28**, 229–236, https://doi.org/10.1175/WAF-D-12-00096.1.

Strader, S. M., and W. S. Ashley, 2018: Finescale assessment of mobile home tornado vulnerability in the central and southeast United States. *Wea. Climate Soc.*, **10**, 797–812, https://doi.org/10.1175/WCAS-D-18-0060.1.

Straka, J. M., and J. R. Anderson, 1993: Numerical simulations of microburst-producing storms: Some results from storms observed during COHMEX. *J. Atmos. Sci.*, **50**, 1329–1348, https://doi.org/10.1175/1520-0469(1993)050<1329:NSOMPS>2.0.CO;2.

Thompson, R. L., R. Edwards, J. A. Hart, K. L. Elmore, and P. Markowski, 2003: Close proximity soundings within supercell environments obtained from the Rapid Update Cycle. *Wea. Forecasting*, **18**, 1243–1261, https://doi.org/10.1175/1520-0434(2003)018<1243:CPSWSE>2.0.CO;2.

——, C. M. Mead, and R. Edwards, 2007: Effective storm-relative helicity and bulk shear in supercell thunderstorm environments. *Wea. Forecasting*, **22**, 102–115, https://doi.org/10.1175/WAF969.1.

——, B. T. Smith, J. S. Grams, A. R. Dean, and C. Broyles, 2012: Convective modes for significant severe thunderstorms in the contiguous United States: Part 2: Supercell and QLCS

tornado environments. *Wea. Forecasting*, **27**, 1136–1154, https://doi.org/10.1175/WAF-D-11-00116.1.

Tirone, E., S. Pal, W. A. Gallus Jr., S. Dutta, R. Maitra, J. Newman, E. Weber, and I. Jirak, 2024: A machine learning approach to improve the usability of severe thunderstorm wind reports. *Bull. Amer. Meteor. Soc.*, **105**, E623–E638, https://doi.org/10.1175/BAMS-D-22-0268.1.

Vermeire, B. C., L. C. Orf, and E. Savory, 2011: Improved modelling of downburst outflows for wind engineering applications using a cooling source approach. *J. Wind Eng. Ind. Aerodyn.*, **99**, 801–814, https://doi.org/10.1016/j.jweia.2011.03.003.

Wakimoto, R. M., 1985: Forecasting dry microburst activity of the high plains. *Mon. Wea. Rev.*, **113**, 1131–1143, https://doi.org/10.1175/1520-0493(1985)113<1131:FDMAOT>2.0.CO;2.

——, and V. N. Bringi, 1988: Dual-polarization observations of microbursts associated with intense convection: The 20 July storm during the MIST project. *Mon. Wea. Rev.*, **116**, 1521–1539, https://doi.org/10.1175/1520-0493(1988)116<1521:DPOOMA>2.0.CO;2.

——, C. J. Kessinger, and D. E. Kingsmill, 1994: Kinematic, thermodynamic, and visual structure of low-reflectivity microbursts. *Mon. Wea. Rev.*, **122**, 72–92, https://doi.org/10.1175/1520-0493(1994)122<0072:KTAVSO>2.0.CO;2.

Weiss, S. J., J. A. Hart, and P. R. Janish, 2002: An examination of severe thunderstorm wind report climatology: 1970–1999. Preprints, *21st Conf. on Severe Local Storms*, San Antonio, TX, Amer. Meteor. Soc., 11B.2, https://doi.org/10.1016/j.foreco.2006.01.032.

Wheeler, M., and S. M. Spratt, 1995: Forecasting the potential for central Florida microbursts. NOAA Tech. Memo. NWS SR-163, 12 pp., https://repository.library.noaa.gov/view/noaa/7286/noaa_7286_DS1.pdf.

Wilson, J. W., R. D. Roberts, C. Kessinger, and J. McCarthy, 1984: Microburst wind structure and evaluation of Doppler radar for airport wind shear detection. *J. Climate Appl. Meteor.*, **23**, 898–915, https://doi.org/10.1175/1520-0450(1984)023<0898:MWSAEO>2.0.CO;2.

——, J. A. Moore, G. B. Foote, B. Martner, A. R. Rodi, T. Uttal, and J. M. Wilczak, 1988: Convection Initiation and Downburst Experiment (CINDE). *Bull. Amer. Meteor. Soc.*, **69**, 1328–1347, https://doi.org/10.1175/1520-0477(1988)069<1328:CIADE>2.0.CO;2.

Woodall, C. W., C. H. Perry, and P. D. Miles, 2006: The relative density of forests in the United States. *For. Ecol. Manage.*, **226**, 368–372, https://doi.org/10.1016/j.foreco.2006.01.032.